

1 **Liver-specific Mettl14 deletion induces nuclear heterotypia and dysregulates RNA export**
2 **machinery**

3
4 Keith A Berggren¹, Saloni Sinha², Aaron E Lin¹, Michael P Schwoerer¹, Stephanie Maya¹,
5 Abhishek Biswas^{1,3}, Thomas R Cafiero¹, Yongzhen Liu¹, Hans P Gertje⁴ Saori Suzuki^{1†}, Andrew
6 R. Berneshawi^{1‡}, Sebastian Carver¹, Brigitte Heller¹, Nora Hassan², Qazi Ali², Daniel Beard¹,
7 Danyang Wang⁵, John M Cullen⁶, Ralph E Kleiner⁵, Nicholas A Crossland^{4,7}, Robert E
8 Schwartz^{2,8,9}, Alexander Ploss^{1*}

9
10 ¹ Department of Molecular Biology, Princeton University, Princeton, NJ, USA.

11 ² Department of Medicine, Weill Cornell Medicine, NY, USA.

12 ³ Research Computing, Office of Information Technology, Princeton University, Princeton, NJ,
13 08544, USA.

14 ⁴ National Emerging Infectious Diseases Laboratories, Boston University, Boston, MA, 02118,
15 USA.

16 ⁵ Department of Chemistry, Princeton University, Princeton, NJ 08544, USA.

17 ⁶ Department of Population Health and Pathobiology, North Carolina State University College of
18 Veterinary Medicine, Raleigh, NC 27607, USA.

19 ⁷ Department of Pathology and Laboratory Medicine, Boston University Chobanian & Avedisian
20 School of Medicine, Boston, MA, 02118, USA.

21 ⁸ Department of Physiology, Biophysics, and Systems Biology, Weill Cornell Medicine, NY,
22 USA.

23 ⁹ Department of Biomedical Engineering, Cornell University, Ithaca, NY, USA.

24 * **Corresponding Author** (aploss@princeton.edu)

25 † Present address: Department of Microbiology and Immunology, Hokkaido University, Japan.

26 ‡ Present address: Stanford University School of Medicine, Stanford, CA, USA.

27
28
29
30
31
32
33
34
35
36
37
38
39
40
41
42
43

44 **Abstract**

45 Modification of RNA with N⁶-methyladenosine (m⁶A) has gained attention in recent years as a
46 general mechanism of gene regulation. In the liver, m⁶A, along with its associated machinery,
47 has been studied as a potential biomarker of disease and cancer, with impacts on metabolism,
48 cell cycle regulation, and pro-cancer state signaling. However these observational data have yet
49 to be causally examined *in vivo*. For example, neither perturbation of the key m⁶A writers *Mettl3*
50 and *Mettl14*, nor the m⁶A readers *Ythdf1* and *Ythdf2* have been thoroughly mechanistically
51 characterized *in vivo* as they have been *in vitro*. To understand the functions of these
52 machineries, we developed mouse models and found that deleting *Mettl14* led to progressive
53 liver injury characterized by nuclear heterotypia, with changes in mRNA splicing, processing
54 and export leading to increases in mRNA surveillance and recycling.

55

56 **Introduction**

57 N⁶-methyladenosine (m⁶A) RNA modification is a critical gene regulatory mechanism, based on
58 extensive *in vitro*, cell culture, and patient studies (1). RNA modification with m⁶A is implicated
59 in cellular differentiation, metabolism, and cell-cycle regulation. Moreover, dysregulation of
60 m⁶A or the m⁶A ‘writer’ enzymes *Mettl3* and *Mettl14* contribute to the development and
61 malignancy of many cancers including hepatocellular carcinoma (HCC) (2–4). Clearly
62 deciphering the impacts of m⁶A modification on the RNAs it is placed on is important, as this
63 modification can lead to either RNA stability in some cases and degradation in others through
64 various mechanisms(5–7). The function of m⁶A on specifically modified transcripts, and the
65 associated machinery including *Mettl3* and *Mettl14* are important to understand not just for
66 diagnostic and prognostic utility, but also as potential causative mechanisms which could serve
67 as therapeutic targets. This interest, along with availability of better tools, has recently led to a
68 flurry of studies on the impacts of disrupting m⁶A writers in liver tissue *in vivo* in mouse models
69 (8–11).

70

71 RNA modification by m⁶A has been implicated in liver diseases, inflammation, and injury
72 response, as well as viral infection (1). Metabolically associated steatohepatitis (MASH) has
73 been correlated with global increases in m⁶A as well as increased levels of writer complex
74 proteins *Mettl14* and *Mettl3* (12). Specific sites on interferon (IFN) beta mRNA have been
75 shown to bear m⁶A modifications, and knockdown of *Mettl14* leads to increased IFN expression
76 and interleukin-17RA, concurrently with increased inflammatory pathway activation and
77 metabolic reprogramming in the liver (13, 14). m⁶A modification of viral RNAs has also been
78 reported on hepatitis B and delta virus RNAs, appearing to impact the viral replicative cycle and
79 the switch from translation of protein and replication to packaging (15, 16). Hepatitis B Virus
80 (HBV) has also been shown to increase m⁶A levels in liver, causing a feed-forward loop of
81 inflammation and leading towards PTEN and innate immunity changes which lead towards HCC
82 development(17).

83

84 Despite this wealth of observational data, it has been difficult to pinpoint causal or mechanistic
85 roles for m⁶A or its associated machinery. First, new studies have cast doubt on the accuracy and
86 reproducibility of commonly used m⁶A sequencing techniques (18). Second, recent work has
87 provided evidence for unexpected feedback loops where m⁶A-modification leads to chromatin
88 remodeling (19). Third, m⁶A writers may have alternate functions, acting directly on DNA or
89 impacting RNA splicing, nuclear export, and localization (20–25). Taken together, these data are

90 difficult to integrate into a comprehensive understanding of how dysregulation of m⁶A and its
91 associated machinery might contribute to or cause liver disease *in vivo*.

92
93 To better understand the effects of m⁶A modification machinery dysregulation in the context of
94 liver tissue, we generated a mouse model of hepatocyte-specific deletion of m⁶A writer *Mettl14*
95 to assess transcriptomic changes in the liver during mature steady-state tissue maintenance. We
96 additionally developed a dual-deletion model of the ‘reader’ proteins *Ythdf1* and *Ythdf2* to
97 disentangle the impacts of the canonical pathway of m⁶A-modified mRNA degradation from
98 other potential outcomes of *Mettl14* deletion. Since the impacts of m⁶A modification are
99 particularly important to temporal regulation of cellular differentiation and cell-cycle regulation
100 during development or regeneration, we also assessed regenerative capacity and liver
101 architecture following an extensive array of injury models: surgical, chemical, or chronic
102 infection. Deletion of *Mettl14* or *Ythdf1/Ythdf2* together led to worse liver outcomes, depending
103 on the type of challenge, highlighting the important roles and different functions of these genes
104 in liver homeostasis and regeneration.

105

106 **Results**

107 **m⁶A machinery defects impact post-natal liver maintenance, leading to injury**

108 To study the impacts of *Mettl14* deletion on proper liver development, we developed a
109 hepatocyte-specific deletion of *Mettl14* via a cross of mice in which exons 7-9 are flanked by
110 loxP sites (*Mettl14*^[fl/fl]) (26) with mice bearing a Cre transgene under the hepatocyte-specific
111 albumin promoter (Alb-Cre) (27) (**Fig. 1A**). We further developed a hepatocyte-specific dual
112 *Ythdf1* and *Ythdf2* deletion mouse by crossing full-body *Ythdf1* knockout (*Ythdf1*^{-/-}) mice with
113 *Ythdf2* floxed (*Ythdf2*^[fl/fl]) mice (26). The subsequent mice were crossed with the Alb-Cre
114 expressing mice to establish dual knockout in hepatocytes (**Fig. 1A**). These liver-specific
115 deletions were necessary as whole-body knockouts of *Mettl14* or *Ythdf2* are embryonic lethal
116 (28, 29). We confirmed reduced *Mettl14* transcript and protein levels in the *Mettl14*^[fl/fl] Alb-Cre
117 liver tissue by reverse-transcription qPCR and western blot, respectively (**Fig. S1E,F**).

118

119 The liver-specific deletion mice appeared grossly normal, although some liver-specific *Mettl14*
120 individuals displayed lower weights and slowed growth (**Fig S1C**). We initially collected tissues
121 from these mice at 8 weeks of age to assess impacts on mature liver development and
122 maintenance by histology imaging of hematoxylin and eosin (H&E)-stained sections. Both the
123 dual *Ythdf1*^{-/-}/*Ythdf2*^[fl/fl]/Alb-Cre and the *Mettl14*^[fl/fl]/Alb-Cre mice showed liver injury with
124 histological similarity to steatohepatitis, but *Mettl14*^[fl/fl]/Alb-Cre mice showed additional
125 inflammation, regions of necrosis, and signs of liver fibrosis (**Fig. 1B**). Deletion of either *Ythdf1*
126 (in the whole animal) or *Ythdf2* (specifically in the liver) on its own did not lead to any
127 significant histological changes (**Fig S1A**).

128

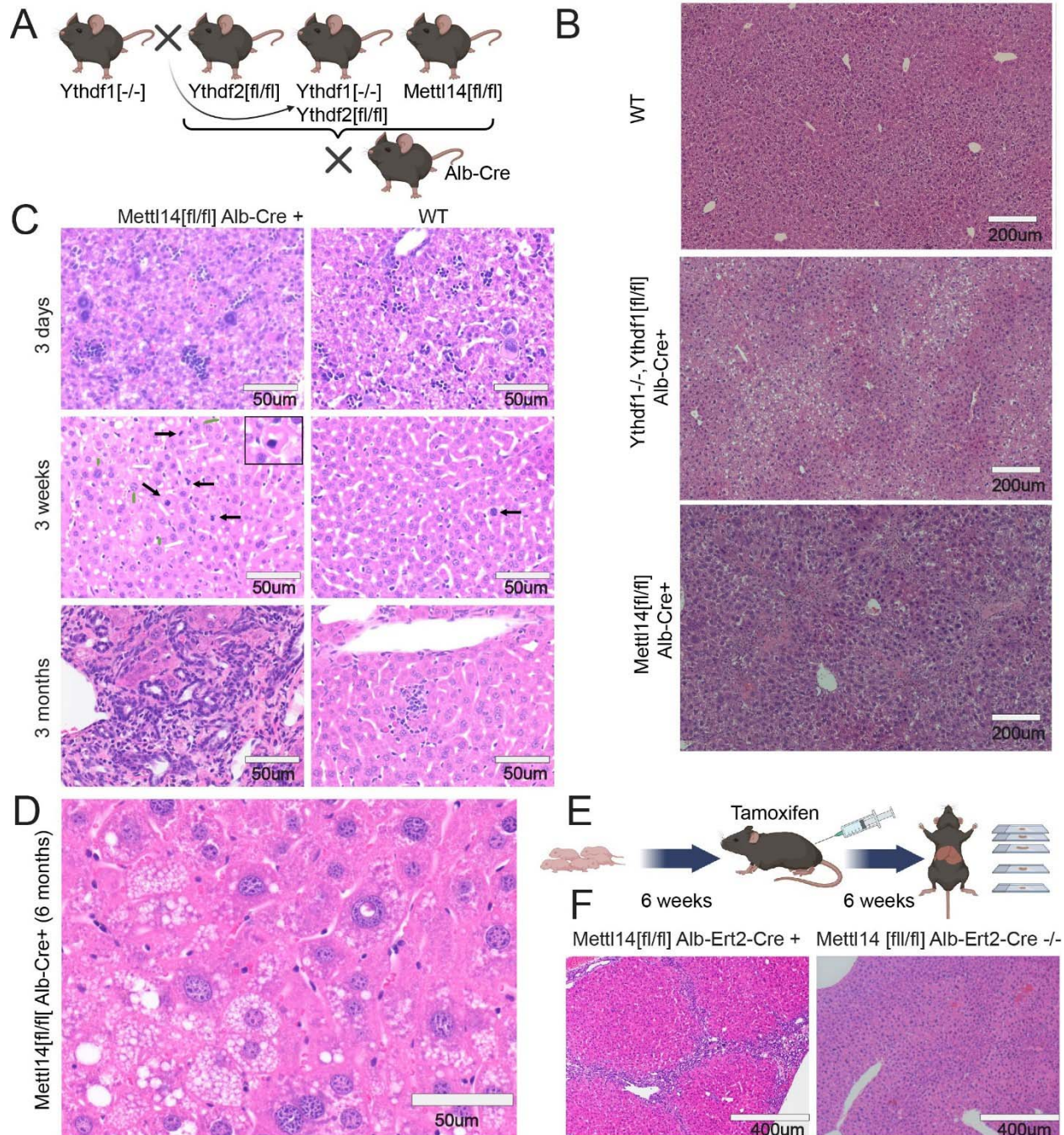


Fig. 1. m⁶A writer and reader deficiencies lead to progressive liver damage. (A) Schematic showing crosses used to generate gene deletions in hepatocytes for this study (Created with BioRender.com). (B) Dual *Ythdf1/Ythdf2* deletion in liver tissue as well as *Mettl14* deletion leads to liver injury, but each with distinctly different histology. (C) *Mettl14*-deficient liver tissue exhibits progressive damage emerging first at 3 days and progressing in severity through 3 months of age and older. Black arrows indicate apoptotic cells with condensed nuclei, green arrows indicate enlarged nuclei, and white arrows indicate mitotic events. (D) Representative image of the advanced liver injury phenotype seen in 6-month-old *Mettl14* deficient liver tissue, showing steatosis and nuclear heterotopia. (E) Schematic of tamoxifen-induction timeline where mice were injected with tamoxifen over 6 weeks before sacrifice for experiments (Created with

129

130

131

132

133

134

135

136

137

138

139

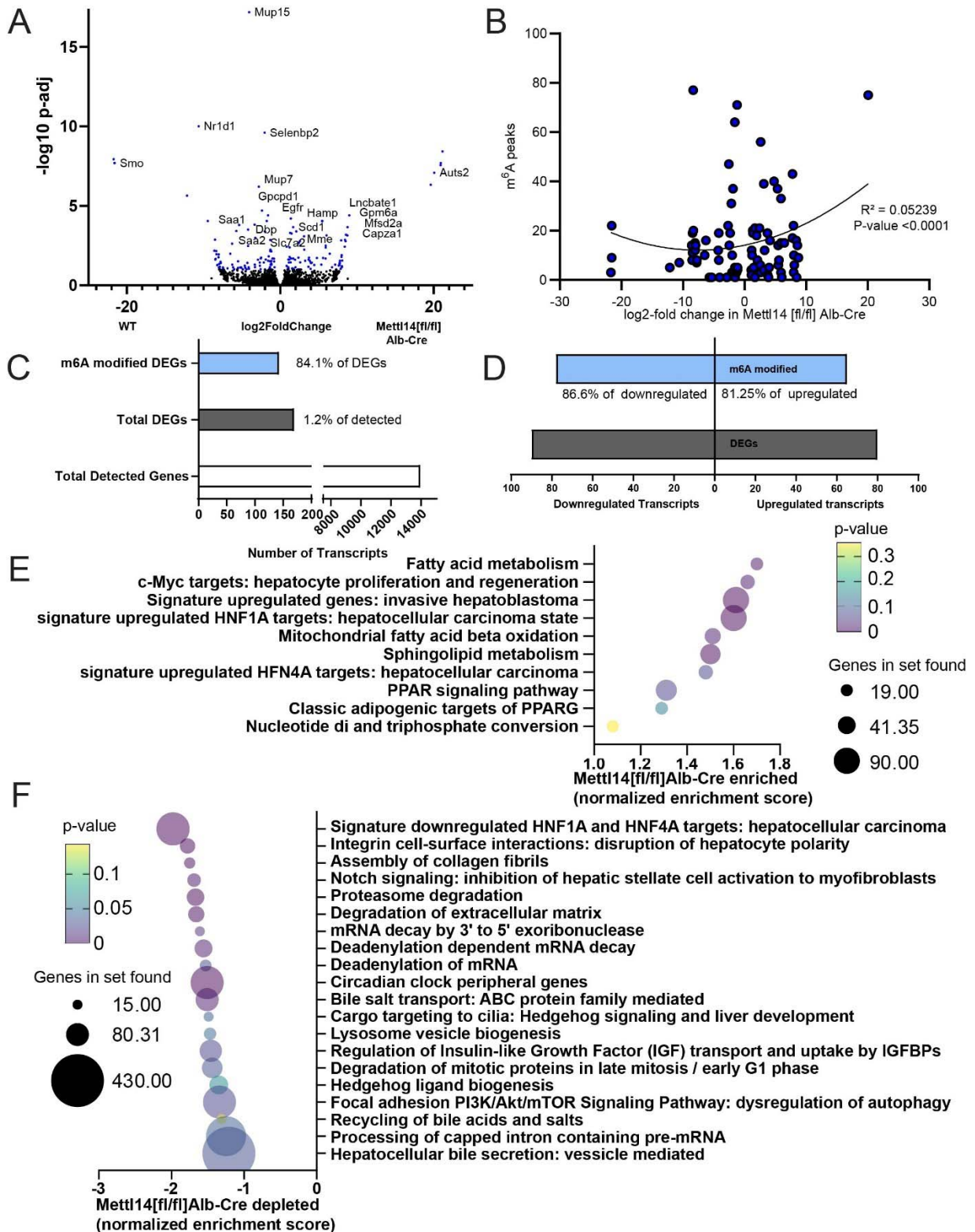
140 BioRender.com). **(F)** Liver injury is recapitulated in this inducible *Mettl14* model, showing
141 similar levels of fibrosis and nuclear heterotypia.

142
143 To assess the timeframe of onset of this damage in *Mettl14*-deleted mice, we analyzed liver
144 tissue architecture of *Mettl14*^[fl/fl]/Alb-Cre mice during growth and maturation (postnatal day 3,
145 week 3, and month 3). By 3 weeks of age, individual hepatocytes could be seen undergoing
146 apoptosis, and the rate of mitotic events was increased relative to the wild-type control (**Fig. 1C**),
147 likely to replace the dying cells. This damage progressed over time, with *Mettl14*^[fl/fl]/Alb-Cre
148 livers at 3 months of age displaying pronounced immune infiltrate and signs of fibrosis. This
149 liver injury phenotype, while variable, was worse in males than females (**Fig. S1D**): male liver
150 injury steadily progressed to a stark phenotype of advanced steatohepatitis with immune infiltrate
151 and pronounced nuclear heterotypia by 6 months of age (**Fig. 1D**). More broad areas of fibrosis
152 and further necrosis and apoptosis can also be seen in mice at older ages (**Fig. S1B**).

153
154 We aimed to characterize global molecular changes underlying the liver pathology observed in
155 *Mettl14*-deleted mice. We performed bulk-RNA sequencing of liver tissue from *Mettl14*^[fl/fl]/Alb-
156 Cre and *Mettl14*^[fl/fl] mice (**Supplemental data 1**). A volcano plot showed good distribution of
157 upregulated and downregulated transcripts, with a relatively low percentage of genes
158 differentially expressed at statistically significant levels (**Fig. 2A**). We compared the set of
159 mRNA transcripts with number of known m⁶A modification sites per transcript with our list of
160 differentially expressed genes and found a correlation between modification and upregulation of
161 transcripts (**Fig. 2B**). Differentially expressed genes (DEGs) represented approximately 1% of
162 the total detected genes (**Fig. 2C**), and 84% of DEGs were known to be m⁶A modified at one or
163 more sites, with a slight skew towards down-regulated genes (30) (**Fig. 2D**).

164
165 Gene set enrichment analysis (GSEA) revealed dysregulation of pathways that confirmed our
166 histological findings of liver pathology (**Supplemental Data 2**). Livers of *Mettl14*-deleted mice
167 had major lipid metabolism and stress response dysregulation, modulated by hepatocyte nuclear
168 factor 1 alpha (*Hnf1a*) and *Hnf4a*. The phenotypes of these GSEA pathways, fibrosis and pro-
169 hepatocellular carcinoma states approximated the steatohepatitis we observed in our mice (**Fig.**
170 **2E,F**) (31–33). Notably, *Smoothened* (*Smo*), a member of the *Hedgehog* signaling pathway,
171 showed remarkably decreased expression in liver tissue from *Mettl14*^[fl/fl]/Alb-Cre as compared
172 to *Mettl14*^[fl/fl] mice. *Smo* transcript expression was not detected in any knockout mouse samples
173 (**Fig. 2A, Fig. S2**), which correlated with *Hedgehog* pathway signaling changes seen in the
174 GSEA (**Fig. 2E,F**). *Smo* and *Hedgehog* signaling have direct impacts on hepatic insulin
175 resistance and metabolism regulation, and decreased *Hedgehog* signaling is correlated with
176 increased susceptibility of fatty liver disease progression to metabolically associated
177 steatohepatitis (MASH) and fibrosis (34–36), similar to the phenotype observed in our mice.

178



180 **Fig. 2. Bulk RNAseq and GSEA analysis reveal key pathways of liver damage.** (A) Volcano
181 plot of transcripts upregulated and downregulated between *Mettl14*^[fl/fl]/Alb-Cre and *Mettl14*^[fl/fl]
182 male mice (n = 3). Hits with a significant adjusted p-value below 0.1 are highlighted in blue.
183 Specific genes with particularly significant p-values or high levels of up-regulation or down-
184 regulation, as well as those with particularly interesting functions to pathways seen in the GSEA
185 are marked with gene names next to their data points. (B) Comparison of known m⁶A modified
186 sites on transcripts with significantly upregulated or downregulated transcripts in *Mettl14*
187 deletion mice. (C) The ratio of enrichment of transcripts published to be m⁶A modified versus
188 those without evidence for modification among differentially expressed genes (DEGs) seen in
189 our data (D) and breakdown of m⁶A enrichment among DEGs in those upregulated and
190 downregulated. (E) Gene set enrichment analysis (GSEA) of bulk transcriptomic data, revealing
191 which pathways and functions are over-represented in the *Mettl14* deletion mice. (F) GSEA
192 results of which pathways and functions are downregulated in *Mettl14* deletion mice.

193

194 To determine whether the damage seen in *Mettl14* mice is due to defects in pre-natal
195 development versus post-natal metabolism and maintenance defects, we separately developed a
196 liver-specific inducible *Mettl14* deletion mouse by crossing our *Mettl14*^[fl/fl] mice with a
197 tamoxifen-inducible Cre, termed Alb-ERT2-Cre (37) expressed under the albumin promoter. At
198 6 weeks of age, we induced gene-specific deletion in these *Mettl14*^[fl/fl]/Alb-ERT2-Cre mice with
199 tamoxifen for a total of 6 weeks to allow time for any potential resulting effects to be
200 histologically evident before sacrificing mice for histological analysis (Fig. 1E). Our results
201 showed that inducible *Mettl14* deletion for 6 weeks in adulthood lead to similar fibrosis and
202 necrosis as was seen in the constitutive deletion model at 6 weeks of age (Fig. 1F). Therefore,
203 we concluded that *Mettl14* was required for proper post-natal liver growth and maintenance.

204

205 **Functional liver regeneration is impeded in *Ythdf1/Ythdf2* dual deletion**

206 The liver possesses an impressive capacity for regeneration after injury, reconstituting not only
207 tissue mass, but also the specific functional architecture of liver tissue with zonation around
208 portal vein tracts and bile ducts (38, 39). This allows rapid response to injury, toxicity, or acute
209 infection to maintain the scope of liver function necessary to maintain metabolic processes. In
210 wild-type C57BL/6 mice, liver regeneration occurs over a period of approximately seven days
211 after experimentally induced injury via two-thirds partial hepatectomy (40). This process
212 requires tight temporal control of cell-cycle, motility, differentiation, and coordination of
213 developmental pathways to reconstitute tissue architecture. All of these processes have been
214 shown in various settings to be impacted or directly regulated by m⁶A modification as a
215 mechanism of gene regulation (41–45). As we initially showed that faulty m⁶A machinery affects
216 liver maintenance at steady-state conditions, we wanted to further know whether m⁶A
217 perturbation would also affect liver regeneration.

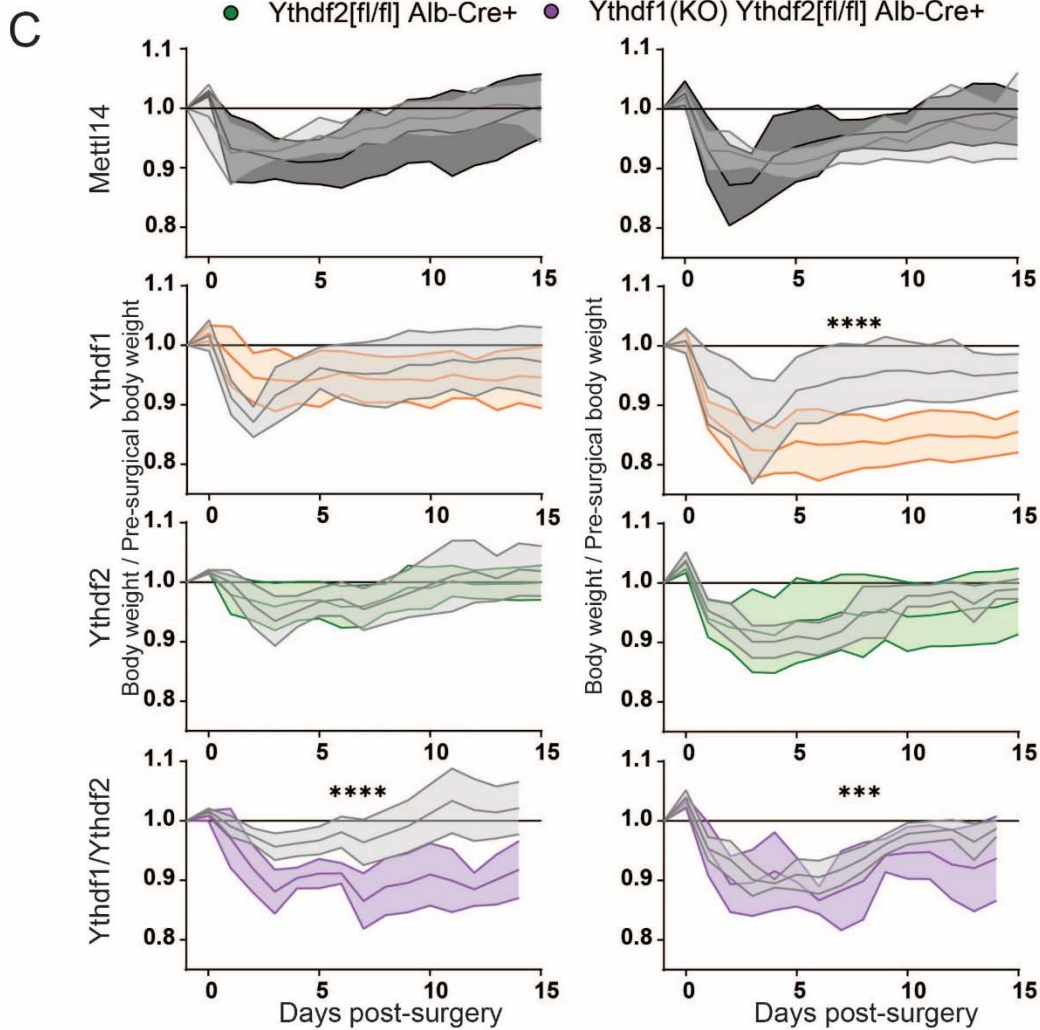
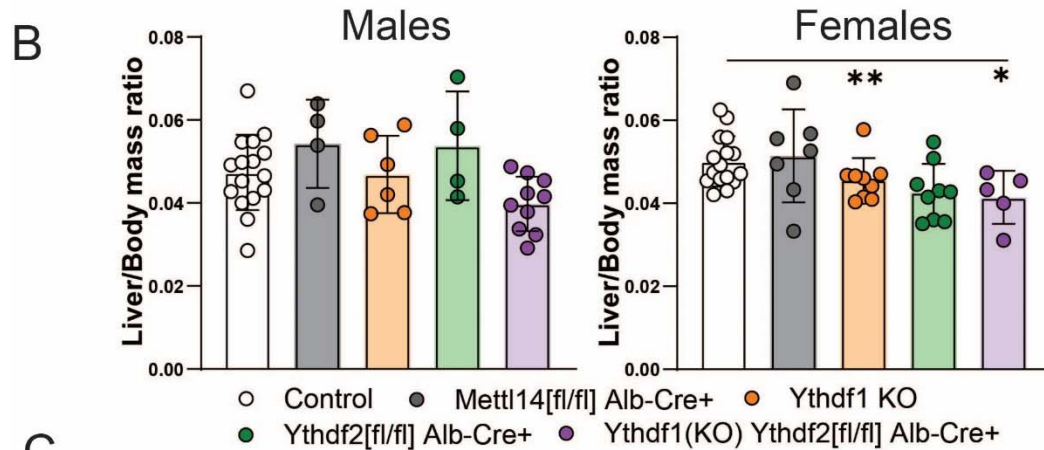
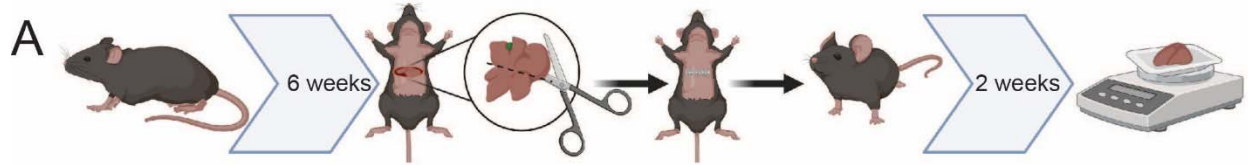
218

219 To better understand the impacts of m⁶A and its readers following injury, we assessed the
220 capacity of *Mettl14*, *Ythdf1*, *Ythdf2*, and dual *Ythdf1/Ythdf2* deficient mice to recover after two-
221 thirds partial hepatectomy surgery. We weighed mice at 6 weeks of age, and then performed
222 surgery to remove approximately two-thirds of total liver mass (Fig. 3A). Tissue was weighed
223 after removal to confirm the appropriate amount of tissue loss. Any individual animals who
224 experienced significant blood loss, deviated significantly from the target amount of tissue
225 removed, or who experienced post-surgical complications were removed from the study to avoid

226 skew of results due to any surgical technique variability. We assessed two phenotypes: (1) liver
227 mass, as a function of the liver's ability to regenerate, and (2) whole body mass, as reduced liver
228 function leads to slower weight recovery. We weighed mice daily for 2 weeks post-surgery
229 before sacrificing them for experimental sample collection and analysis. Total liver mass was
230 assessed at time of sacrifice and compared as a ratio of liver mass to body mass to control for
231 relative variability in overall animal size.

232

233 In *Ythdf1*^{-/-}/*Ythdf2*^[fl/fl]/Alb-Cre and *Ythdf1*^{-/-} mice, overall liver mass regeneration was
234 significantly reduced compared to control animals after surgery (**Fig. 3B**). An expected sexual
235 dimorphism in regenerative capacity was also noted, with males regenerating more liver tissue
236 than females of the same genotype (46). As a proxy of liver function, the whole body weight of
237 *Ythdf1*^{-/-}/*Ythdf2*^[fl/fl]/Alb-Cre mice recovered significantly more slowly, irrespective of sex (**Fig.**
238 **3C**). Deficiency of *Ythdf1* alone also resulted in significantly reduced weight recovery in female
239 mice. The close agreement between which groups displayed significant reduction of regenerated
240 liver mass and overall weight recovery was noted. These results suggest that deletion of the
241 reader genes *Ythdf1* and *Ythdf2* slowed liver regeneration and function following surgical injury.



243 **Fig. 3. Significantly slower liver regeneration in m⁶A reader-deficient mice following**
244 **partial hepatectomy. (A)** Schematic of timeline for two-thirds hepatectomy surgery and
245 recovery prior to sacrifice and sample collection (Created with BioRender.com). **(B)** Males (left)
246 and females (right): comparison of liver /body mass ratios at 2 weeks post-surgery across
247 C57BL/6 (N=16 males, 16 females) *Mettl14* (N=4 males, 7 females), *Ythdf1* (N=6 males, 9
248 females), *Ythdf2* (N=4 males, 9 females), and dual *Ythdf1/Ythdf2* deletion mice (N=10 males, 5
249 females). **(C)** Males (left) and females (right): weight recovery curves after surgery.

250

251 **Acute liver injury is exacerbated by m⁶A reader or writer deletion**

252 Different type of liver damage can reveal different aspects of injury response and recovery.
253 Probing these m⁶A reader and writer deficient mice with experimental liver injury allows us to
254 better understand the actual nature of their defects and chronic injury phenotypes. Two separate
255 toxicity-based injury models of liver damage response are used frequently in liver research to
256 assess response to cholestasis-mediated liver injury as well as general hepatocyte toxicity. 1,4-
257 dihydro 2,4,6-trimethyl 3,5-pyridinedicarboxylic acid diethyl ester (DDC) administration causes
258 protoporphyrin plugs and stones, blocking bile ducts and impeding bile drainage from the liver
259 parenchyma (47). This leads to cholestasis as bile buildup damages cholangiocytes, leading to
260 sclerosing cholangitis and biliary fibrosis. A second model of liver injury is carbon tetrachloride
261 (CCl₄). CCl₄ directly damages hepatocytes by inducing a severe state of oxidative stress by
262 binding to triacylglycerols and phospholipids, leading to lipid peroxidation (48). These two
263 distinctly different modalities of liver injury were used here as models to assess liver injury
264 response to both post-necrotic hepatocellular fibrosis and cholestatic biliary fibrosis. In the
265 context of our hepatocyte-specific deletion models, this allows us to probe the differences
266 between hepatocyte response to direct damage, and response to cholangiocyte damage leading to
267 liver injury.

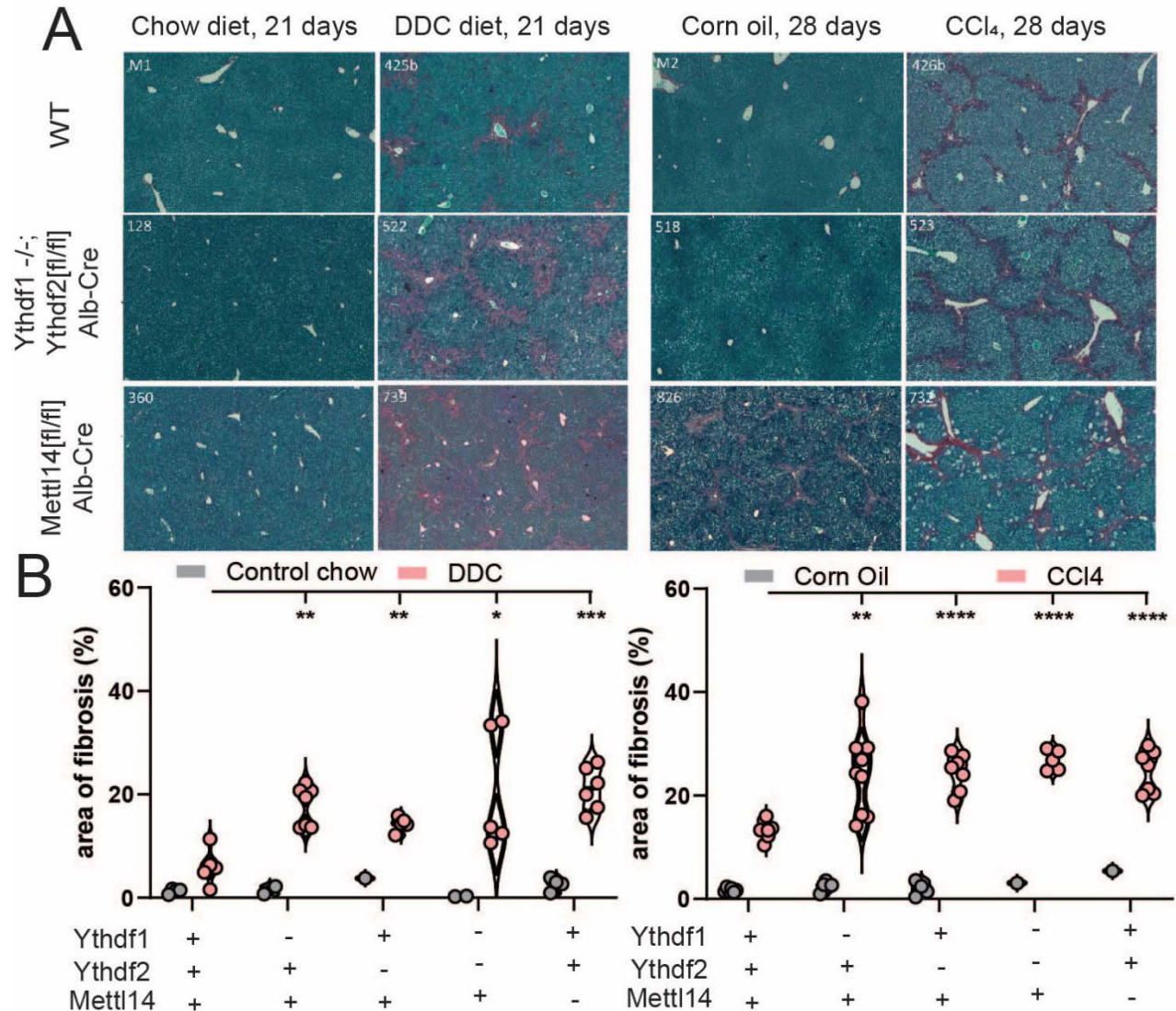
268

269 We compared livers from control-chow and DDC-chow fed animals of each previously described
270 genotype after 21 days of treatment. Histology of picosirius red-stained liver sections displayed
271 increased fibrosis in all m⁶A-perturbed genotypes relative to wild-type (**Fig. S3A**). Dual
272 *Ythdf1/Ythdf2* deficient livers developed extensive fibrosis bridging from bile ducts to portal vein
273 tracts (**Fig. 4A**). *Mettl14* deficient livers exhibit some fibrosis even in mock-treated conditions
274 but developed bridging fibrosis as well as general diffuse fibrosis throughout the bulk of the
275 tissue under DDC treatment (**Fig. 4A**, left). Quantification of the area of fibrosis staining by
276 picosirius red shows that all genotypes (*Ythdf1*^{-/-}, *Ythdf2*^[fl/fl]/Alb-Cre, dual *Ythdf1*^{-/-}
277 */Ythdf2*^[fl/fl]/Alb-Cre, and *Mettl14*^[fl/fl]/Alb-Cre) progress to a significantly higher level of fibrosis
278 than wild-type mice under DDC treatment, but dual *Ythdf1/Ythdf2*- and *Mettl14*-deficient mice
279 both exhibited the highest-percentage areas of fibrosis (**Fig. 4B**, left). Quantification of blocked
280 bile ducts in DDC treated liver tissue show ductular reaction and response to injury. In our model
281 mice, *Mettl14* mice recovered similarly to wild-type mice, while *Ythdf1/Ythdf2* mice showed
282 significantly reduced numbers of unblocked bile ducts per HPF (**Fig. S3B**).

283

284 We similarly analyzed tissues from mice after 28 days of CCl₄ treatment. All genotypes
285 displayed increased fibrosis relative to control wild-type mice, with evident bridging fibrosis
286 (**Fig. S3C**). Dual *Ythdf1/Ythdf2* deficient mice showed pervasive bridging fibrosis throughout the
287 liver, and histologic analysis of *Mettl14* deficient mice revealed foci of necrosis throughout the
288 liver in addition to the fibrosis (**Fig. 4A**, right). Automated image analysis demonstrated that

289 while the percent area of fibrosis was increased in all perturbed genotypes relative to wild type,
 290 the dual *Ythdf1/Ythdf2* deficient mice had the highest average percent area of fibrosis after CCl₄
 291 treatment, with just over 25% of all liver tissue area staining positive for fibrosis (**Fig. 4B**, right).
 292 The number of mitotic cells counted per high-powered microscope field (HPF) was significantly
 293 elevated relative to wild type mice in *Ythdf1* and *Ythdf2* mice, but not *Mettl14* mice (**Fig. S3D**).
 294 Therefore, deletion of either the readers or writers led to worse liver injury following direct
 295 damage to hepatocytes or indirect damage via bile duct blockade.

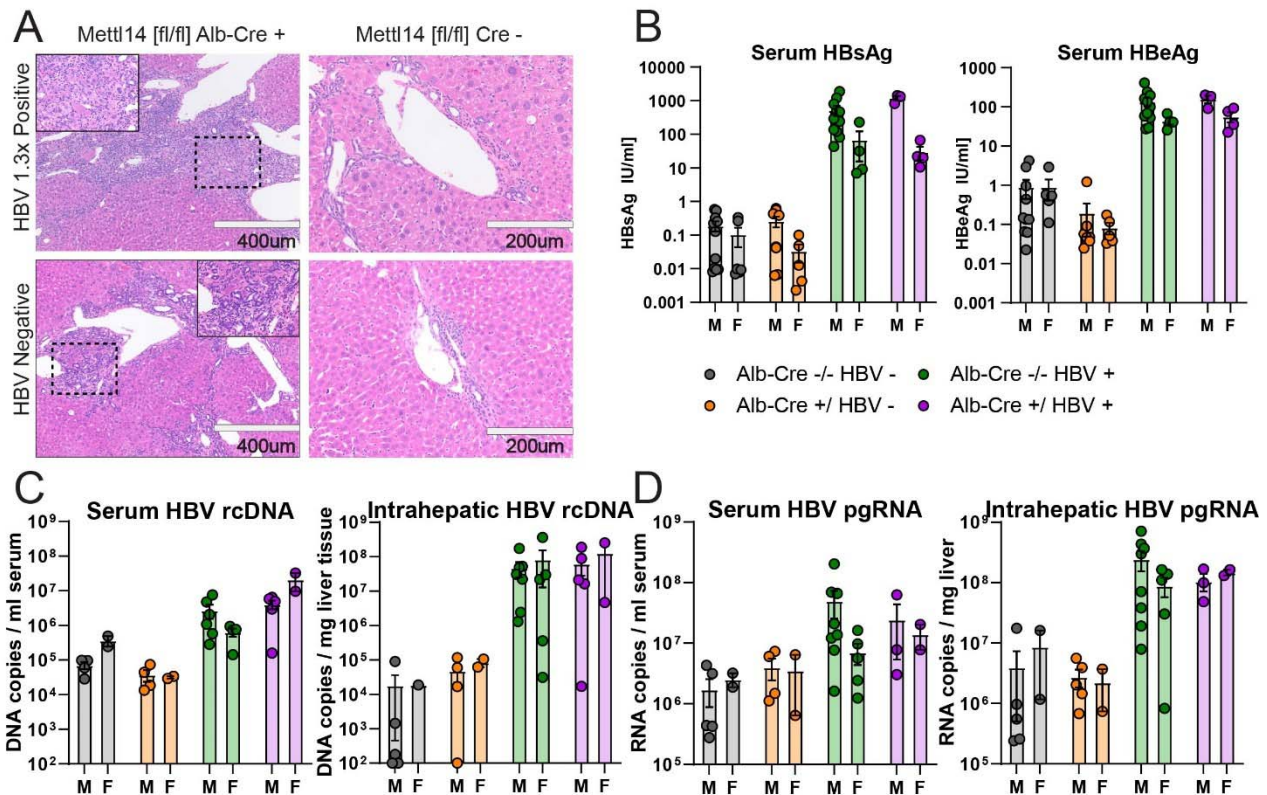


296 **Fig. 4. m⁶A reader and writer deficiency increases liver fibrosis response to toxicity.**
 297 (A) Histological staining with picosirius red of mock (chow diet) and DDC diet-treated (left)
 298 male mice reveals increased liver injury and areas of fibrosis (red). Similar staining of mock
 299 (corn oil) and CCl₄-treated male mice (right) reveals the same pattern of liver injury and fibrosis
 300 advancement in m⁶A reader- and writer-perturbed mice. (B) Quantitative image analysis of areas of
 301 fibrosis in DDC diet- (left) and CCl₄- (right) treated mice with mock comparison.
 302
 303

304 **HBV genome induced hepatic inflammation is worsened in *Mettl14* deficient mice**

305 Chronic HBV infection is a major cause of liver fibrosis and progression to hepatocellular
 306 carcinoma (49). Given the known role of both m⁶A and HBV in HCC development and
 307 progression, and the known role of m⁶A on HBV replication cycle and protein translation, we
 308 were interested in whether disruption of m⁶A modification in *Mettl14*^[fl/fl]/Alb-Cre mice would
 309 impact outcomes of HBV exposure (15, 50–52).

310
 311 To assess the potential changes in HBV replication, translation, and injury, we crossed our
 312 *Mettl14*^[fl/fl]/Alb-Cre mice with mice bearing the HBV 1.3x length genome as a transgene (1.3x
 313 HBV tg). These mice produce all gene products of HBV and produce packaged viral particles
 314 (53). To allow time for significant liver injury to accumulate, we waited until 3 months of age to
 315 subject tissues from these animals for analysis. Histological comparison of H&E-stained sections
 316 showed that while HBV expression leads to some minor injury and inflammation, HBV
 317 expression in *Mettl14*^[fl/fl]/Alb-Cre mice exacerbates hepatic injury and fibrosis beyond that
 318 normally seen in *Mettl14*^[fl/fl]/Alb-Cre mice (Fig. 5A). Bridging fibrosis was noted with
 319 especially broad regions of fibrosis and immune infiltrate bridging between portal vein tracts and
 320 bile ducts.
 321



322
 323 **Fig. 5. *Mettl14* deficiency impacts liver injury but not HBV translation or replication.**
 324 (A) Histology of H&E-stained sections from male *Mettl14*^[fl/fl]/Alb-Cre and *Mettl14*^[fl/fl] control
 325 mice expressing HBV 1.3x genome transgene, and comparison with control HBV negative mice.
 326 (B) ELISA assays showing blood serum HBsAg (left) and HBeAg (right) protein levels of HBV
 327 expressing mice in comparison to control HBV negative animals to establish baseline. (C) qPCR
 328 of HBV genomic rcDNA extracted from blood serum (left) and liver tissue (right). (D) RT-qPCR
 329 of HBV pre-genomic RNA extracted from blood serum (left) and liver tissue (right).

330

331 To assess the level of packaged and released viral particles in the blood, we collected serum from
332 blood samples and measured HBV S antigen (HBsAg) levels by ELISA assay. This antigen is an
333 integral part of secreted subviral and infectious HBV particles. We found no significant
334 difference between either males or females expressing HBV with and without *Mettl14* defects
335 (**Fig. 5B**, left). We further quantified HBV E antigen (HBeAg) levels in blood serum, a marker
336 of ongoing virus replication, by ELISA. We again found no significant differences in HBV-
337 expressing mice (**Fig. 5B**, right).

338

339 To thoroughly assess levels of viral replication and transcription, we also quantified levels of
340 HBV genomic relaxed circular DNA (rcDNA) and pre-genomic RNA (pgRNA) in both serum
341 and liver tissue by (RT)qPCR. There was no significant difference in rcDNA levels among
342 *Mettl14*^[fl/fl]/Alb-Cre/1.3x HBV tg and *Mettl14*^[fl/fl]/1.3x HBV tg control mice in liver tissue or
343 serum (**Fig. 5C**). Similarly, we saw no significant differences in pgRNA in either serum or liver
344 tissue (**Fig. 5D**). Collectively, these data demonstrate that while HBV genome expression
345 worsens liver disease in *Mettl14*-deleted mice, which cannot be attributed to elevated levels of
346 HBV replication intermediates or viral proteins.

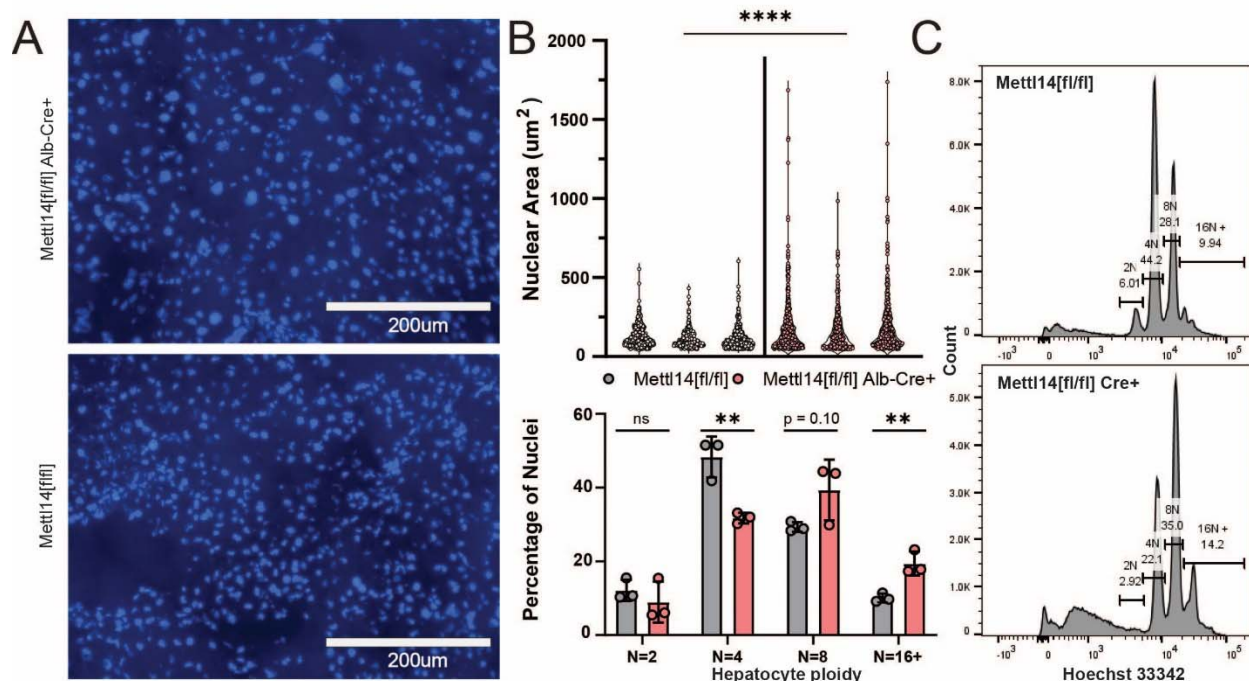
347

348 ***Mettl14* deletion leads to pronounced nuclear heterotypia and increased polyploidy in** 349 **hepatocytes**

350 One striking phenotype caused by *Mettl14* deletion was nuclear heterotypia, which we observed
351 in steady state (**Fig. 1**) and following various injuries. GSEA analysis of transcriptomic analysis
352 of *Mettl14*-deletion mice highlighted several potential explanatory mechanisms of the nuclear
353 heterotypia we observed in these mice (**Fig. 2E,F**). Cell-cycle regulatory pathways of c-Myc
354 signaling, circadian clock-related genes, and late mitosis / early G1 phase cell cycle regulation
355 genes were all dysregulated. RNA metabolism, processing, splicing, and degradation were also
356 evidently disrupted, with upregulated nucleotide di- and tri-phosphate conversion and
357 downregulation of mRNA decay mechanisms including deadenylation, as well as processing and
358 splicing of capped intron-containing pre-mRNA.

359

360 Dysregulation of cell cycle, RNA processing and export, as well as signs of oxidative stress can
361 all lead towards nuclear heterotypia. To confirm our original histological H&E staining and
362 perform further quantification of the nuclear heterotypia to better describe the phenotype and
363 narrow down potential contributing mechanisms, we stained liver sections from *Mettl14*-deletion
364 and wild-type mice with Hoechst-33342 (**Fig. 6A**). Quantitative image analysis across 3
365 individuals of each group showed that there was a significant increase in the mean size and size
366 variability of nuclei in *Mettl14*-deletion liver (**Fig. 6B**, top). To assess any change in polyploidy
367 occurring alongside nuclear size changes we isolated nuclei from liver tissue samples and
368 performed flow cytometry, which showed a marked shift of hepatocyte ploidy towards 8n and
369 higher ploidies (**Fig. 6B**, bottom). Representative histograms of Hoechst-33342 signal from the
370 flow cytometry data collection show clear separation between each peak, indicating distinct
371 populations of nuclei (**Fig. 6C**).



372
 373 **Fig. 6. *Mettl14* deletion-related nuclear heterotopia is concurrent with increased ploidy**
 374 (A) Hoechst-3342-stained histological sections reveal an increase in nuclear size in *Mettl14*
 375 deletion mice (top) relative to wild type control mice (bottom). (B) Quantitative analysis (top) of
 376 imaging data from separate animals shows consistently increased nuclear size and greater range
 377 of size in *Mettl14*^[f/f]/Alb-Cre mice vs *Mettl14*^[f/f] controls. Quantitative analysis of hepatocyte
 378 ploidy via flow cytometry (bottom) of Hoechst-33342 stained hepatocyte nuclei. (C)
 379 Representative histograms of Hoechst-33342 staining intensity from flow cytometry data of
 380 stained hepatocyte nuclei.

381
 382 **Nuclear accumulation of the TREX complex member *Alyref* reveals impacts of *Mettl14* on**
 383 **RNA trafficking machinery**

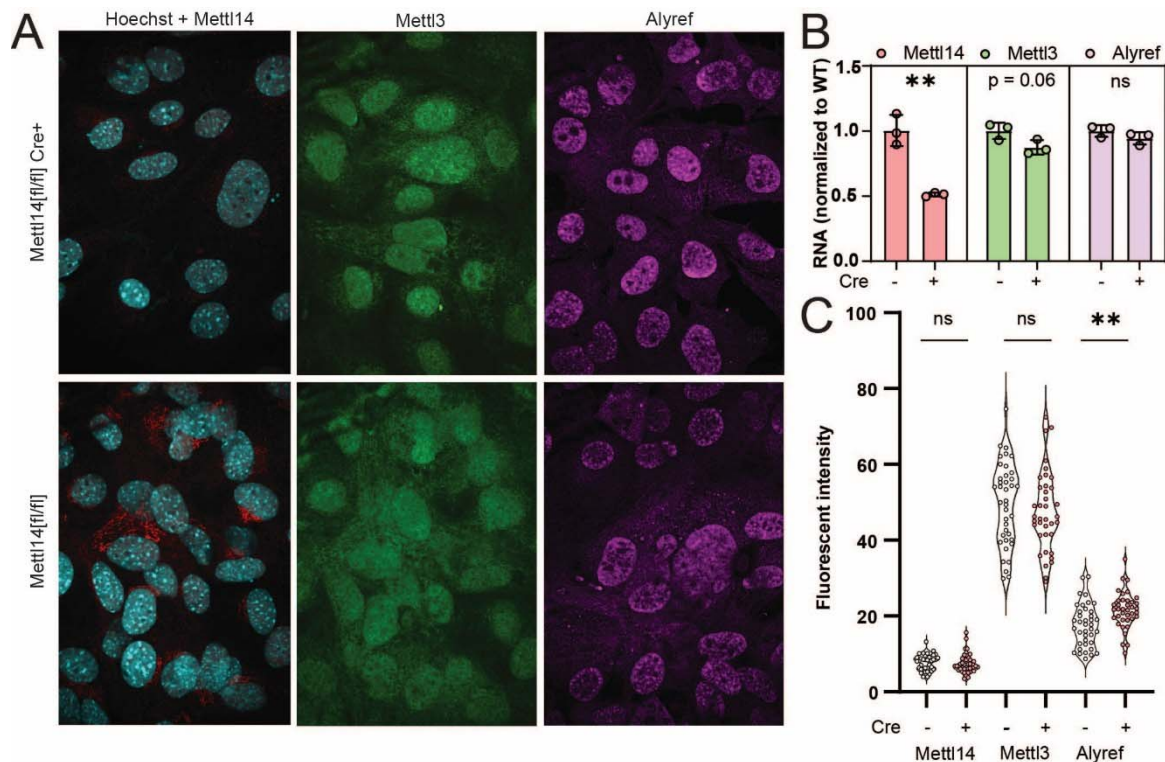
384 To gain more mechanistic insight into the nuclear heterotopia phenotype, we further explored the
 385 results of our gene set enrichment analysis of our transcriptomic data. We observed upregulation
 386 of mRNA splicing, trafficking, and activation for translation, as well as pathways involved in
 387 metabolic and oxidative stress, mitochondrial biogenesis, apoptosis, and fatty acid oxidation
 388 (Fig. 5E,F). RNA metabolism, processing, splicing, and degradation were also evidently
 389 disrupted, with upregulated nucleotide di- and tri-phosphate conversion and downregulation of
 390 mRNA decay mechanisms including deadenylation, as well as processing and splicing of capped
 391 intron-containing pre-mRNA. We further saw that cell-cycle regulatory pathways of circadian
 392 clock-related genes, and late mitosis / early G1 phase cell cycle regulation genes were all
 393 dysregulated.

394
 395 We identified a number of differentially expressed transcripts with direct ties to the m⁶A
 396 machinery (Fig. S2). In *Mettl14*^[f/f]/Alb-Cre mice, we found upregulation of *Brf2*, *R3hdm4*,
 397 *Taf1a*, and *Zfp747*, among other genes which play roles in RNA transcription initiation and
 398 regulation. We also saw upregulation of *Srpk1*, a key member involved in spliceosomal complex

399 assembly which is responsible for mRNA processing, splicing, and export processes which all
 400 assemble within nuclear speckles. Notably, the transcription/export complex (TREX), which is
 401 the major mechanism of mRNA nuclear export in a m⁶A, assembles on m⁶A modified mRNAs
 402 via binding to the m⁶A modifying machinery within nuclear speckles (21, 23). Therefore, we
 403 wondered whether *Mettl14*-deletion might dysregulate the mRNA export machinery, in turn
 404 leading to nuclear heterotopia, cell cycle defects, and liver pathology.

405
 406 To test the TREX mechanism of m⁶A-related mRNA export suggested by the transcriptomic
 407 data, we wanted to quantify the nuclear concentration of the key TREX complex member
 408 Aly/REF export factor (*Alyref*). Since liver tissue produces high autofluorescence that interferes
 409 with immunofluorescence, we instead derived a mouse embryonic fibroblast line from
 410 *Mettl14*^[fl/fl] mice, and stably transduced them with both simian virus 40 (SV40) large T antigen.
 411 To disrupt *Mettl14*, we transduced a population of cells with Cre expressing lentivirus and
 412 compared them to cells without Cre (Fig. S4A). *Mettl14* was efficiently deleted in the presence
 413 of Cre, as judged by confocal microscopy (Fig. 7A), reverse transcription qPCR (Fig. 7B), and
 414 western blot (Fig. S4B), while the other m⁶A writer *Mettl3* was unaffected. Though *Alyref*
 415 mRNA levels were unchanged (Fig. 7B), *Mettl14*-deletion led to an increase in nuclear *Alyref*
 416 protein levels (Fig. 7A,C). These data support a mechanism by which *Mettl14* deletion alters
 417 nuclear mRNA export machinery, causing downstream effects on nuclei, cell cycle, and liver
 418 injury.

419
 420
 421



422
 423 **Fig. 7. TREX complex localization changes reveal RNA trafficking machinery defects**
 424 (A) Representative images from *Mettl14*^[fl/fl]/Cre (top) and *Mettl14*^[fl/fl]/Cre MEFs (bottom) show
 425 differences in *Mettl14* signal in red (left), *Mettl3* signal in green (middle) and TREX complex

426 marker *Alyref* in pink (right). (B) RT-qPCR data show gene expression of *Mettl14* is
427 significantly reduced approximately 50%, but *Mettl3* and *Alyref* levels are unchanged. (C)
428 Quantitative analysis of multiple replicate slides showing nuclear localized signal by co-
429 localization with Hoechst-33342 signal demonstrates an increase in nuclear *Alyref* signal.

430

431 Discussion

432 Many experimental studies in cell culture and observational clinical studies have shown that
433 disruption of normal m⁶A modification impacts a layer of gene regulation leading to defects in
434 cell-cycle regulation and important metabolic processes; however, it has been challenging to
435 experimentally study these effects *in vivo*, as full-body knockouts of the key m⁶A writers and
436 readers are embryonic lethal (4, 11, 12, 54). Here, we generated and thoroughly characterized
437 novel mouse models with liver-specific genetic ablation of *Mettl14*, *Ythdf2*, and dual
438 deletion of *Ythdf1* and *Ythdf2*. Though these mice are viable, both *Mettl14* and dual
439 *Ythdf1/Ythdf2* deletion causes their livers to undergo progressive injury with steatohepatitis, and
440 in the case of *Mettl14*, nuclear heterotypia, which can be further exacerbated by surgical,
441 chemical, and infectious challenges. This suggests a critical role for m⁶A in post-natal liver
442 maintenance and regeneration.

443

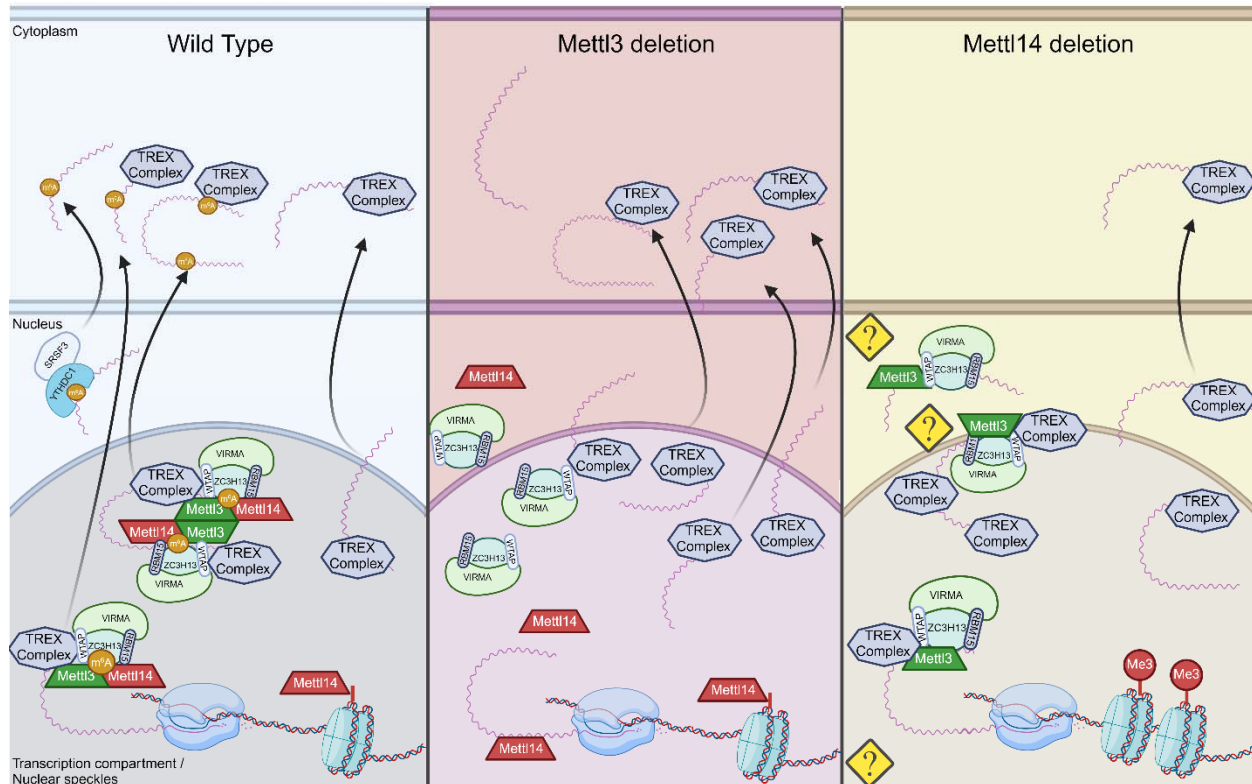
444 We leveraged transcriptomic data to identify dysregulated nuclear mRNA export as a potential
445 molecular mechanism driving nuclear heterotypia. *Mettl14*^[n/m]/Alb-Cre mice showed significant
446 changes in abundance of transcription, splicing, and nuclear export machinery mRNA. Recent
447 literature has shown that TREX mediated mRNA export is enhanced by m⁶A modification of
448 mRNAs, with direct TREX complex binding m⁶A modification machinery scaffold proteins vir
449 like m⁶A methyltransferase associated (*Virma*) and WT associated protein (*Wtap*) (21, 23).
450 Disruption of the m⁶A modification complex was shown to significantly impact the ratio nuclear
451 to cytosolic abundances of known m⁶A modified transcripts, but not control transcripts without
452 m⁶A sites. Assembly of the m⁶A complex occurs dynamically within phase-separated nuclear
453 speckles, colocalizing with the TREX complex assembly and binding (22). This phase separation
454 is driven by *Mettl3* when bound to *Mettl14* during assembly, but *Mettl3* homodimerization can
455 drive phase separation and assembly in the absence of *Mettl14* (22). *Mettl14* is not capable of
456 driving the same phase separation, even when homodimerization is forced by experimental
457 fusion protein expression (22).

458

459 *Mettl3* self-interaction is normally capable of driving phase separation and assembly of the m⁶A
460 modification machinery complex, which along with WTAP binding, promotes phase separation
461 of the mRNA bound complex (22). This phase separation puts the m⁶A complex-bound mRNA
462 in close contact with TREX complex, promoting binding and nuclear export via *Nxf1* recruitment
463 and mRNA handover. Simultaneously, m⁶A modified mRNAs are recognized by *Ythdc1*, leading
464 to export via *Srsf3* binding (55). TREX complex members, along with potentially other mRNA
465 export factors, shuttle back and forth from nucleus to cytoplasm to affect mRNA export (21, 23).
466 TREX binding to non-m⁶A modified transcripts also leads to mRNA export, but through binding
467 at alternate sites, leading to low efficiency of export of normally m⁶A modified transcripts (23).
468 *Mettl14* plays a *Mettl3*-independent role in chromatin openness through direct interaction with
469 H3K27me3 and recruiting *Kdm6b* to induce H3K27me3 demethylation (56). This promotes
470 transcription, with *Mettl14*, but not *Mettl3* deletion exhibiting a global decrease in transcription

471 rate, which promotes binding to the TREX complex within phase separated nuclear speckles.
 472 These bound complexes are likely not properly bound to mRNAs due to the absence of *Mettl14*.
 473

474 Taken together with our data, this suggests a possible mechanism of mRNA trafficking defects
 475 unique to *Mettl14* deletion models not seen under *Mettl3* deletion (**Fig. 8**). Perturbation of the
 476 above mechanisms in *Mettl14* deficient cells results in nuclear sequestration of the associated
 477 TREX complex via some potential mechanism of association with m⁶A machinery components
 478 in the absence of *Mettl14* (**Fig. 8, right**). Specifically, the reports of *Mettl3* self-interaction and
 479 association with *Wtap* driving phase separation of bound complex, and the known role of *Mettl3*
 480 in binding to the TREX complex (22, 23), nuclear retention of RNAs in *Mettl14* deletion (57)
 481 and our current report of TREX nuclear sequestration in *Mettl14* deletion together could all
 482 contribute to differences in outcome of *Mettl3* deletion and *Mettl14* deletion models via *Mettl14*
 483 independent interaction of *Mettl3*. This would lead not only to dysregulation of normally m⁶A
 484 modified transcripts, but all transcripts which utilize the TREX mechanism of nuclear export.
 485



486 **Fig. 8. Proposed mechanisms for nuclear maintenance of TREX in *Mettl14* deletion**
 487 In wild-type cells (left), *Mettl3* and *Mettl14* function as a complex to place m⁶A modifications on
 488 mRNA transcripts. In *Mettl3*-deficient cells (middle), export of normally m⁶A-modified
 489 transcripts is slowed, but transcription rates are maintained or increased, allowing alternate
 490 pathways of TREX-mediated mRNA export to function at capacity (56). In *Mettl14*-deficient
 491 cells, m⁶A-mediated mechanisms of mRNA export are impaired similarly to *Mettl3* deletion, but
 492 TREX complex shuttling is also impaired through nuclear retention by mechanisms not yet
 493 understood. At the same time, global transcription rates are impacted by loss of *Mettl14*
 494 chromatin binding (Created with BioRender.com).
 495

496

497 At the same time, pre-mRNAs are not properly m⁶A modified, reducing the processes of mRNA
498 splicing and processing, and leading to increased nuclear mRNA surveillance recognition and
499 degradation of these overabundant and improperly spliced pre-mRNAs, as seen represented in
500 our data presented here. Furthermore, the co-opting of the mRNA surveillance and degradation
501 pathways might competitively inhibit this process from regulating other pre-mRNAs which
502 might be frequently alternatively spliced or improperly processed as a regulatory mechanism.
503 Overactivation of mRNA degradation and nucleotide scavenging processes due to mRNA
504 processing and trafficking machinery defects could also lead to a cascade of apoptotic, stress,
505 and immune responses which could contribute to nuclear heterotypia and overall liver damage.

506
507 Significant changes in *Hedgehog*, *PPAR γ* , *c-Myc*, and *PI3K/mTOR/Akt* signaling axes were
508 detected and impacts of m⁶A on signaling deserve special consideration in follow-up work. In
509 particular, *Smo* mRNA has been found in several studies to have multiple m⁶A modification
510 sites, and expression is likely regulated by this mechanism (30). Our GSEA results confirmed the
511 important dysregulation of *Hedgehog* signaling, with several gene sets involved not just with
512 *Smo* itself, but also *Hedgehog* ligand synthesis and trafficking pathways significantly reduced
513 (Fig. 2E,F). Noted changes to overall lipid metabolism and subsequent pre-diabetic and pro-
514 fibrotic responses as well as cell cycle dysregulation leading towards an HCC like state are all
515 observed possible downstream effects of *Hedgehog* signaling dysregulation (34–36). Our
516 transcriptomics data showed changes in ciliary trafficking of *Hedgehog* signaling ligands, despite
517 hepatocytes lacking cilia. Taken together with the significant changes in bile acid salt
518 metabolism and secretion, there are likely changes in *Hedgehog* signaling cholangiocytes and
519 potentially between hepatocytes and peri-biliary portal fibroblasts (58).

520
521 The results of this study merit follow-up work investigating this model mechanism. Changes in
522 *Mettl14* and m⁶A modification abundances have been widely reported and considered as disease
523 biomarkers in various liver diseases including MASH and HCC, and work is ongoing for
524 potential therapeutic applications targeting *Mettl14* and overall m⁶A regulation (1, 2, 59, 60). It is
525 therefore urgent that we understand the outcomes of changes to *Mettl14* and *Mettl3* expression *in*
526 *vivo* thoroughly, both together and in isolation, to inform drug target development. The scope of
527 bulk-RNAseq limits this study, and follow-up studies utilizing spatial transcriptomics would
528 strengthen our understanding of the role of *Hedgehog* signaling. This signaling occurs both
529 within hepatocytes and between hepatocytes, peri-biliary portal fibroblasts, and cholangiocytes.
530 Understanding this signaling more thoroughly would allow us to understand the contribution of
531 non-hepatocyte cell types in general in this liver-injury state in *Mettl14* deletion. Follow-up work
532 could also clarify the transcriptomic and proteomic state of *Mettl14* deletion mice at earlier
533 timepoints during the initial onset of liver injury, and of the dual *Ythdf1*^{-/-}/*Ythdf2*^[fl/fl]/Alb-Cre
534 mouse model in comparison to *Mettl14* deletion to further confirm and specify the gene
535 dysregulation responsible for the differences in injury phenotypes.

536 537 **Materials and Methods**

538 539 **Experimental Design**

540 Experiments were designed to specifically assess the impacts of m⁶A within the context of an *in*
541 *vivo* system. Mouse models for study were obtained as described in the relevant materials and
542 methods section below. Study of the steady state impacts in adult mice was conducted initially

543 via histologic analysis of H&E stained liver sections to determine any gross defects, and assess
544 the nature of any evident changes. Due to the evident gross morphologic changes in *Mettl14*
545 deficient liver tissue, we aimed to fully characterize the nature of the defects by determining
546 whether this injury was due to improper liver organogenesis and development, or tissue
547 maintenance and metabolism defects. To distinguish between these two effect types, we
548 performed similar histology analysis of *Mettl14* model mice over a time course of early post-
549 natal development. Simultaneously, we developed an inducible model of gene deletion for
550 *Mettl14*, described in the relevant materials and methods section, to clearly exclude any
551 developmental effects from impacting tissue architecture or damage. Our subsequent
552 experimental designs were focused on two specific questions: the roles of m⁶A machinery
553 components in injury response and regeneration, and the mechanisms leading to the unique
554 nuclear heterotopia phenotype seen specifically in *Mettl14* deletion liver tissue.

555
556 To further probe the roles of m⁶A machinery components in injury response and regeneration,
557 we imposed a suite of injuries and insults to the liver with various mechanisms of damage.
558 Physical injury was induced via two-thirds partial hepatectomy, while chemical injury to
559 hepatocytes was modeled by CCl₄ treatment. DDC was utilized to model cholestatic disease via
560 injury by blocking bile ducts. Finally, we modeled components of chronic hepatitis B infection
561 by developing an HBV expressing *Mettl14* deficient mouse line. While the HBV expressing
562 mouse model does not fully model chronic infection, as these animals are tolerized to HBV and
563 express the genome themselves rather than supporting true viral infection, aspects of chronic
564 HBV infection such as HBV protein toxicity are represented in this model.

565
566 To better understand the mechanisms underlying the nuclear heterotopia observed in *Mettl14*
567 deletion liver tissue, we first aimed to characterize the state of these mice by transcriptomic
568 analysis. To get better data on any changes of nuclear localization, nuclear heterotopia was
569 further explored by flow cytometry analysis of hepatocyte nuclei ploidy. Since this can skew the
570 data, as larger nuclei may be more fragile and less likely to be cleanly isolated from liver tissue,
571 image analysis of confocal images of liver sections was used to quantify the nuclei size
572 distribution *in situ*. Finally, due to the high autofluorescence background making antibody-based
573 fluorescent imaging difficult in liver tissue, we derived a mouse embryonic fibroblast line with
574 similar levels of *Mettl14* knockdown in order to image subcellular localization and expression
575 levels of *Mettl14*, *Mettl3*, and *Alyref*, a component of the TREX mRNA transcription and export
576 complex.

577 **Mice**

578 C57BL/6 and B6.Cg-^{Tg(Alb-cre)21Mgn/J} (Alb-cre) were obtained from the Jackson Laboratory (Bar
579 Harbor, ME) (27). *Mettl14*^[fl/fl], *Ythdf1*^{-/-} and *Ythdf12*^[fl/fl] (all on the C57BL/6 background)
580 were kindly provided by Dr. Chuan He (University of Chicago, HHMI) (26) Alb^{tm1(cre/ERT2)Mtz} by
581 Dr. Pierre Chambon (INSERM, Université Louis Pasteur) (37) and 1.3x HBV transgenic mice
582 by Dr. Frank Chisari (Scripps Research) (61). *Mettl14*^[fl/fl]/Alb-Cre, *Ythdf2*^[fl/fl]/Alb-Cre and
583 *Ythdf2*^[fl/fl]/Alb-Cre *Ythdf1*^{-/-}, *Mettl14*^[fl/fl]/Alb-ERT2-Cre, *Mettl14*^[fl/fl]/Alb-Cre/1.3x HBV tg mice
584 were generated by intercrossing mice harboring the respective alleles and typing offspring with
585 primer combinations distinguishing wild-type and mutant alleles (typing information are
586 available upon request).

588

589 Animal experiments were performed in accordance to a protocol (number 3063) reviewed and
590 approved by the Institutional Animal Care and Use Committee (IACUC) at Princeton University
591 and in accordance to IACUC protocol 2016-0047 reviewed and approved by the Weill Cornell
592 Medical College IACUC.

593

594 **Tamoxifen induction experiments**

595 Tamoxifen induction of Alb-ERT2-Cre expressing mice was performed using a protocol adapted
596 from the Jackson Laboratory. Tamoxifen (Sigma-Aldrich, St. Louis, MO) was dissolved in corn
597 oil at a concentration of 20 mg/ml by shaking overnight at 37°C. Tamoxifen solution was
598 administered by intra-peritoneal injection at a dose of approximately 75 mg/kg body mass, a
599 standard dose of 100 ul per mouse. 5 days of consecutive once daily administration were
600 performed to induce recombination, followed by once weekly injection for 6 weeks of total time
601 before animals were sacrificed for experimental analysis. All materials, animal bedding, and
602 waste was handed appropriately to avoid exposure of personnel.

603

604 **Histology**

605 During sample collection, mouse livers were perfused with PBS (Life Technologies, Carlsbad,
606 CA) using a BD Vacutainer SafetyLok butterfly needle 23 gauge, 2/4" needle length, 12" tubing
607 length (Becton, Dickinson and Company, Franklin Lakes, NJ) via the portal vein prior to
608 removal to clear the liver tissue of blood and achieve cleaner histology sections. Samples were
609 collected and placed in 4% [w/vol] PFA prepared from a 10% [w/vol] neutral buffered formalin
610 solution (Sigma-Aldrich, St. Louis, MO) for fixation prior to paraffin embedding for histologic
611 sectioning and staining.

612

613 Samples from DDC and CCl₄ experiments were sent to Saffron Scientific Histology Services,
614 LLC (Carbondale, IL) for paraffin-embedding and hematoxylin and eosin (H&E) or Picrosirius
615 Red staining.

616

617

618 Separate samples were placed in OCT in plastic cassettes and frozen at -20°C. Cryostat
619 sectioning using a CM3050S Cryostat (Leica Biosystems, Wetzlar, Germany) was performed to
620 obtain ~5um thick sections and samples were mounted on glass slides and stained with
621 Hoechst33342 (Invitrogen, Waltham, MA) at 5ug/ml [w/vol] for 30 minutes at room temperature
622 prior to being sealed under glass coverslips with ProLong™ Gold Antifade Mountant
623 (Invitrogen, Carlsbad, CA). These liver-section slides were imaged using a Nikon Ti-E
624 microscope with Spinning Disc and Photomanipulation Module (Minato City, Tokyo, Japan),
625 and nuclear area was analyzed using Fiji image analysis to set regions of interest around the
626 nuclei (62).

627

628 **Partial hepatectomies**

629 After weighing animals and recording pre-operative weight, we conducted surgeries under
630 isoflurane induction of anesthesia. Following approved IACUC protocol (number 3063), we used
631 a surgical technique adapted from Nevzorova et al. to remove 3 lobes from the liver, representing
632 approximately two thirds of liver mass (40). Removed tissue was weighed to confirm the amount
633 of liver mass loss, and the peritoneal wall were closed after application of analgesic medication
634 using discontinuous 4/0 vicryl sutures (Ethicon surgical technologies, Bridgewater, NJ). Skin

635 was closed using surgical wound clips (Stoelting, Wood Dale, IL) rather than sutures to prevent
636 wound re-opening from animals licking or chewing on the incision site. Animals were weighed
637 post-operatively, and daily thereafter, with recorded weights corrected for the weight of surgical
638 staples used. Analgesic medication was administered twice daily, in accordance with the
639 timeframes in the approved protocol. At 2 weeks post-surgery, animals were sacrificed for
640 collection of liver samples and analysis.

641

642 **DDC and CCl₄ toxicity experiments**

643 Mice arriving from Princeton University were housed in the quarantine facility of Weill Cornell
644 Medicine for 6 weeks before being used for liver injury experiments. All mice were under a 12-
645 hour light: dark cycle with free access to regular food and water. Mice used for fibrosis or injury
646 models were used at ages 10-12 months unless otherwise indicated.

647 For CCl₄ experiments, mice received biweekly injections of 25% [w/vol] CCL4 (Sigma-Aldrich,
648 St. Louis, MO), diluted in corn oil at a dose of 2 µl/g, for a total of 4 weeks. 0.1% [w/w] 3,5-
649 diethoxycarbonyl-1,4-dihydrocollidine (DDC) (Sigma-Aldrich, St. Louis, MO), was mixed with
650 5053, Purina Picolab Rodent Diet 20 (Envigo, Indianapolis, IN) and given for 21 days. Animals
651 were randomly assigned to groups. Blinding could not be performed given the nature of the
652 experiments. All animal experiments were performed on at least two separate occasions and in
653 accordance with the guidelines set by the Institutional Animal Care and Use Committee at Weill
654 Cornell Medicine and approved in IACUC protocol 2016-0047.

655 Liver tissues were fixed in 4% [vol/vol] paraformaldehyde and sent to Saffron Scientific
656 Histology Services, LLC (Carbondale, IL) for paraffin-embedding and hematoxylin and eosin
657 (H&E), and Picrosirius Red staining. Stained liver sections were observed and imaged using the
658 Axioscan 7 Slide Scanner (Zeiss, Jena, Germany) and analyzed for percent area fibrosis using
659 ImageJ software (<https://imagej.net/ImageJ>).

660

661 **HBV assays**

662 HBsAg and HBeAg antigen levels were quantified as previously described (63) from serum
663 samples obtained by submandibular bleeds of experimental mice. Chemiluminescence
664 immunoassays (CLIA) for both antigens were performed using HBsAg and HBeAg CLIA kits
665 from Autobio Diagnostics (Zhengzhou, Henan, China) according to manufacturer instructions
666 using 50µl of serum.

667

668 HBV rcDNA and pgRNA were extracted from both mouse liver tissue and serum samples using
669 a Quick-DNA/RNA Microprep Plus Kit (Zymo Research, Irvine, CA) following the
670 manufacturer's instructions. Briefly, liver samples and serum samples were resuspended in
671 300 µl DNA/RNA Shield. Liver samples were homogenized using a TissueLyser LT bead mill
672 (Qiagen, Venlo, The Netherlands) for three separate 2 minute cycles followed by digestion with
673 15 µl Proteinase K (20 mg/ml) for 30 min. 300 µl DNA/RNA lysis buffer was then added to
674 both liver and serum samples. Samples were loaded into Zymo-Spin IC-XM columns to collect
675 the DNA and flow-through was saved. An equal volume of ethanol was added to the flow-
676 through to purify RNA by using the Zymo-Spin IC column. Finally, the DNA/RNA was eluted
677 from the columns with 30 µl of nuclease-free water and concentrations were measured using a
678 Nanodrop spectrophotometer (Thermo Fischer Scientific, Waltham, MA).

679

680 HBV rcDNA was quantified from 2 μ l aliquots of HBV DNA isolated either from liver samples
681 or blood serum was used per reaction well. We used a well-characterized HBV rcDNA qPCR
682 system with HBV-qF (nt 1776–1797, numbered based on gt D with GenBank accession no.
683 U95551.1): 5'-GGAGGCTGTAGGCATAAATTGG-3', HBV-qR (nt 1881–1862, numbered
684 based on gt D with GenBank accession no. U95551.1): 5'-CACAGCTTGGAGGCTTGAAC-3'
685 covering the conserved region of HBV(LLD \approx 1.0E⁺ \times 10³ copies/mL) (63). Primers were kept at
686 a final concentration of 500 nM in a 20 μ l reaction volume. On a Step One Plus qPCR machine
687 (Life Technologies), we ran the following program: denature 95 $^{\circ}$ C for 10 min, followed by
688 40 cycles of 95 $^{\circ}$ C for 30 s, 60 $^{\circ}$ C for 30 s, and 72 $^{\circ}$ C for 25 s.

689
690 HBV pgRNA was quantified from HBV RNA extracted from liver tissue or serum as described
691 above. 7.5 μ l of the resultant sample was treated by DNase I (Thermo Fisher Scientific,
692 Waltham, MA, USA) followed by reverse transcription with a specific HBV primer (5'-
693 CGAGATTGAGATCTTCTGCGAC-3', nt 2415–2436, numbered based on gt D with GenBank
694 accession no. U95551.1) located in precore/core region (64) using RevertAidTM First Strand
695 DNA Synthesis Kit (Thermo Fisher Scientific, Waltham, MA, USA). For absolute quantification,
696 standards with 1-mer HBV target template were cloned into the TOPO-Blunt Cloning vector
697 (Thermo Fisher, Waltham, MA, USA #450245) and copy number was calculated based on the
698 vector molecular weight and concentration. A master mix was created containing 15 μ l
699 2 \times Taqman reaction mix (Applied Biosystems, Waltham, MA, USA), 500 nM forward and
700 reverse primers, 200 nM probe and 3 μ l synthesized cDNA in a 30 μ L reaction. This master
701 mix was then added to the samples and 10-fold serial dilution standards and the following
702 cycling program was used to run the qPCR: 95 $^{\circ}$ C for 10 min; 45 cycles of 95 $^{\circ}$ C 15 sec
703 and 58 $^{\circ}$ C for 45 sec.

704 **RT-qPCRs for cellular transcripts**

705 To assess RNA levels of *Mettl14*, *Mettl3*, and *Alyref*, as well as Cre and simian virus 40 (SV40)
706 large T antigen (LT) transgenes, reverse transcription real-time qPCR was performed on RNA
707 samples from mouse liver samples and mouse embryonic fibroblast cell culture samples. All
708 qPCRs were performed using the Luna[®] Universal One-Step RT-qPCR Kit (New England
709 Biolabs, Ipswich, MA) and a Step One Plus qPCR machine (Life Technologies, Carlsbad, CA).
710 *Mettl14* was analyzed using the forward primer (5'- GACTGGCATCACTGCGAATGA-3') and
711 reverse primer (5'- AGGTCCAATCCTTCCCCAGAA-3'). *Mettl3* was measured using the
712 forward primer (5'- CTGGGCACTTGGATTTAAGGAA-3') and reverse primer (5'-
713 TGAGAGGTGGTGTAGCAACTT-3'). *Alyref* was measured using forward primer (5'-
714 GGCACCGTACAGTAGACCG-3') and reverse primer (5'-
715 AAGTCCAGGTTTGACACGAGC-3'). Cre levels were measured using forward primer (5'-
716 GCGGTCTGGCAGTAAAACTATC-3') and reverse primer (5'-
717 GTGAAACAGCATTGCTGTCACTT-3'). LT levels were assessed with forward primer (5'-
718 CTGACTTTGGAGGCTTCTGG -3') and reverse primer (5'- GGAAAGTCCTTGGGGTCTTC
719 -3'). All transcript levels were normalized to housekeeping gene standard GAPDH, which was
720 measured using the forward primer (5'- CCATGGAGAAGGCTGGGGC -3') and reverse primer
721 (5'- ATGACGAACATGGGGGCATCAG -3'). All primers were commercially obtained from
722 Eton Biosciences (San Diego, CA). Standard reaction programs were run using the Step One
723 software and Tm recommendations.

724
725

726 **Transcriptomics**

727 Liver tissue was collected from animals after perfusion with PBS via the portal vein to remove
728 blood from tissue. RNA was extracted from bulk liver tissue using the Monarch total RNA
729 miniprep kit (New England Biolabs, Ipswich, MA) after homogenization with steel beads using a
730 TissueLyser LT bead mill (Qiagen, Venlo, The Netherlands). After extracting total RNA, we
731 verified high-RNA quality by Bioanalyzer RNA Nano/Pico assay (Agilent Technologies, Santa
732 Clara, CA).

733
734 We used 50 ng total RNA per sample for gene expression profiling. We performed bulk RNA-
735 barcoding and sequencing (BRB-Seq) (65) with minor modifications to the reverse transcription
736 (RT) step. We used Template Switching RT Enzyme Mix (NEB, Ipswich, MA), along with a
737 uniquely barcoded oligo(dT)30 primer for each sample, modified to use the Illumina TruSeq
738 Read 1 priming site instead of Nextera Read 1 (66). We performed the remainder of BRB-Seq per
739 protocol: we pooled up to 24 first-strand cDNAs into a single tube, performed Gubler-Hoffman
740 nick translation cDNA synthesis, and tagmented cDNA with in-house-produced Tn5 (67). We
741 amplified cDNAs with 17 PCR cycles using a P5-containing primer and a distinct multiplexed i7
742 indexing primer (Chromium i7 Multiplex Kit, 10X Genomics, Pleasanton, CA). We performed
743 size-selection using sequential 0.55X and then 0.75X SPRIselect (Beckman Coulter, Brea, CA),
744 and sequenced libraries on one lane of a NovaSeq SP v1.5 flowcell (Illumina, San Diego, CA)
745 with 28 cycles Read 1, 8 cycles Read i7, and 102 cycles Read 2.

746 **Nuclei Isolation**

747 Nuclei for and flow cytometry analysis were extracted from frozen liver tissue samples as
748 previously described (68). Briefly, Samples were prepared by incubating freshly obtained liver
749 tissue samples of approximately 1 gram in HypoThermosol® FRS solution (Sigma-Aldrich, St.
750 Louis, MO) for 15 minutes on ice, followed by 30 minutes in CryoStor® CS10 cryopreservation
751 medium (STEMCELL technologies, Vancouver, BC, Canada) on ice. Samples were then frozen
752 overnight at -80 °C in a in a Mr. Frosty cryo-freezing container (Thermo Scientific, Waltham,
753 MA). Tissue was then briefly washed in ice-cold DPBS (Thermo Scientific, Waltham, MA),
754 minced using surgical scissors in a petri dish into small pieces, and homogenized using a glass
755 tissue grinder dounce with the small sized pestle A (DWK Life Sciences, Wertheim, Germany).
756 Nuclei were briefly fixed with 0.1% [w/vol] PFA (Electron Microscopy Sciences, Hatfield, PA)
757 and separated by centrifugation at 500g for 5 minutes. Nuclei were then washed and prepared for
758 downstream applications as appropriate.

760 **Gene set enrichment analysis**

761 Transcriptomic data was analyzed by GSEA software (69, 70). Analyses were performed using
762 the MSigDB M2 curated mouse gene set database (<https://www.gsea-msigdb.org/gsea/msigdb/>).
763 This gene set was chosen since we were looking for specific mechanisms of RNA metabolism or
764 specific steps of metabolism important to liver function and cell cycle regulation, rather than
765 general signaling pathways and pro-cancer gene sets which were strongly represented in other
766 gene set databases such as the hallmark MH gene set database.

768 **Flow cytometry**

769
770

771 Nuclei, isolated as described above, were prepared for flow cytometry by staining with Hoechst-
772 3342 (Invitrogen, Waltham, MA) at 5 μ g/ml [w/vol] for 30 minutes at room temperature,
773 followed by 3 washes in DPBS (Thermo Scientific, Waltham, MA) supplemented with 5% fetal
774 bovine serum. Flow cytometry data collection was performed using an LSRII Flow Cytometer
775 (BD Biosciences). Data were analyzed using FlowJo software (TreeStar).

776

777 **Mouse embryonic fibroblast [MEF] generation**

778 MEFs were generated as previously described (71). Briefly, In brief, the skin biopsies were
779 scraped to remove connective tissue, cut into smaller pieces, and digested overnight at 4°C in
780 HBSS without Ca²⁺ and Mg²⁺ (Thermo Fisher Scientific), containing 1 ml dispase (5,000
781 caseinolytic units/ml; Corning) for every 9 ml of HBSS containing final concentrations of 100
782 mg/ml streptomycin, 100 U/ml penicillin, and 250 ng/ml amphotericin B (HyClone). After
783 digestion, the epidermis was removed and discarded, whereas the remaining dermis was cut into
784 smaller pieces less than a few square millimeters in area. These pieces were moistened with
785 DMEM and pressed into a six-well plate scored with a razor blade. The dermis was maintained
786 in DMEM containing 10% FBS and 1% vol/vol penicillin/streptomycin solution at 37°C, 5%
787 CO₂. Media was changed every 4–5 d and fibroblast growth was typically observed within 1 wk
788 of culture. Once sufficient outgrowth had occurred, the dermis was removed from the plate and
789 the fibroblasts expanded into larger cultures.

790

791 To generate the immortalized dermal fibroblast cell line, γ -retroviral pseudoparticles containing a
792 transfer plasmid encoding Simian virus 40 (SV40) large T antigen were produced in HEK293T
793 cells. Cells were cultured on poly-L-lysine-coated 10 cm plates at 37 °C, 5% (vol/vol) CO₂ in
794 10% FBS DMEM. At ~80% confluency, Xtremegene HP DNA transfection reagent
795 (MilliporeSigma, 6366244001) was used per manufacturer's directions to cotransfect the cells
796 with 4 μ g of pBABE-neo-SV40 large T, a generous gift from B. Weinberg (Addgene plasmid no.
797 1780); 4 μ g of a plasmid containing the genes for Moloney murine leukaemia virus gag-pol; and
798 0.57 μ g of a plasmid containing the gene for the G envelope protein of vesicular stomatitis virus.
799 Supernatants were harvested 24, 48 and 72 h post-transfection, stored at 4 °C then pooled before
800 passing through a 0.45 μ m membrane filter (MilliporeSigma, HAWP02500). Polybrene (Sigma-
801 Aldrich, TR-1003; final concentration, 4 μ g ml⁻¹) and HEPES (Gibco, 15630080; final
802 concentration, 2 mM) were added to the filtered supernatants; aliquots were prepared and at –80
803 °C until needed. Primary dermal fibroblasts were seeded in six-well plates for transduction so
804 that cell confluency was 30–40% at the time of transduction. The cells were 'spinoculated' in a
805 centrifuge at 37 °C, 931 relative centrifugal force (r.c.f.) for 2 h with 2 ml of thawed, undiluted
806 γ -retroviral pseudoparticles per well. The cells were subsequently kept at 37 °C, 5% (vol/vol)
807 CO₂ and the media replaced with 10% FBS DMEM 6 h post-spinoculation. The transduced cells
808 were pooled once they achieved ~80% confluency in the six-well plate and subsequently
809 expanded to prepare immortalized cell stocks. Cells were verified as negative for mycoplasma by
810 testing with the MycoAlert Mycoplasma Detection Assay kit (Lonza, LT07–318) per the
811 manufacturer's instructions.

812

813 To establish the *Mettl14* deficient MEF cell line, MEFs were transduced with VSV-G
814 pseudotyped lentiviral particles expressing CRE recombinase. Lentivirus was generated as
815 described above. The CRE expressing lentiviral backbone was obtained as CSW-CRE plasmid, a
816 generous gift of Dr. Charles M. Rice, The Rockefeller University).

817

818 **Immunofluorescence imaging and Image analysis**

819 MEF cells were seeded and grown overnight on glass coverslips before being fixed with 4% PFA
820 [w/vol.] at room temperature for 30 minutes. After fixation, cells were washed with PBS and
821 then permeabilized at -20°C for 10 min in ice-cold 90% (v/v) methanol. Cells were washed
822 again in PBS and blocked at room temperature for 1 hour with IF buffer [PBS supplemented with
823 10 % (v/v) FBS and 2 mM EDTA]. Cells were incubated overnight at 4°C in primary antibody
824 diluted in IF-T buffer (IF buffer with 0.3 % Triton X-100). The following day, cells were washed
825 three times in IF-T buffer, incubated at room temperature for 1 hour in secondary antibody
826 diluted 1:100 in IF-T buffer, washed three times again, and then imaged with a confocal
827 microscope. A polyclonal antibody was used at 1:500 for *Mettl14* (Invitrogen, Waltham, MA).
828 Monoclonal antibodies were used at 1:250 for *Mettl3* [EPR18810] (Abcam, Cambridge, UK) and
829 *Alyref* [EPR17942] (Abcam, Cambridge, UK).

830

831 The Hoechst-3342 channel from the images was extracted, and Cellpose 2.0 (72) was used to
832 generate segmentation, outlining the nuclei. These outlined nuclei images were then imported
833 into the Tissue Analyzer (73) plugin of Fiji for manual inspection and correction. After
834 corrections, the outline images were transformed into labeled images by assigning a unique label
835 to each pixel within the nuclei boundaries using Python's scikit-image and OpenCV2 libraries.
836 These labeled segmentation masks were utilized to calculate the size and mean intensities for
837 each nucleus across all other channels. This was accomplished through a Python script that
838 iterates over each labeled region, extracting masked pixels and computing their size and mean
839 using NumPy.

840

841 **Western Blot**

842 Cells or liver tissue samples were lysed in ice-cold RIPA buffer [1% Nonidet P-40, 0.5%
843 Deoxycholate, 150 mM NaCl, 50 mM Tris-HCl, pH 7.4, 1.5 mM MgCl₂, 1 mM EGTA, 10%
844 (v/v) glycerol] supplemented with 1x protease inhibitor cocktail (Sigma-Aldrich, St. Louis, MO),
845 spun at 12,000 rpm for 10 min, and pellet discarded. Protein amounts were quantified with a
846 Pierce BCA kit (Thermo Fisher Scientific, Somerset, NJ), mixed with 6x Laemmli buffer, heated
847 at 95°C for 5 min, loaded into a 10% polyacrylamide gel, and ran at 170 V for 1 hour. Gels were
848 transferred to a nitrocellulose membrane with a Genie Blotter (Idea Scientific, Minneapolis,
849 Minnesota), blocked in Tris-buffered saline with 0.1% [v/v] Tween-20 with 5% [w/v] milk for
850 30 min at room temperature, and incubated with primary antibody for 1 hour at 4°C . Membranes
851 were washed three times for 5 min in TBST and incubated for 30 min in either IRDye 680CW or
852 800CW secondary antibodies (Licor, Lincoln, NE) (1:20,000). Imaging was performed with the
853 Li-Cor Odyssey Infrared Imaging System (Licor, Lincoln, NE).

854

855 **Statistical analysis**

856 An unpaired-student's T-test was used to compare groups to wild-type in figures 3B, 4B,
857 5B,C,D, 6B, 7B,C. A paired student's T-test was used to compare weight changes over time to
858 wild-type baseline in partial hepatectomy recoveries in figure 3C. P-values of 0.05 or less were
859 considered significant. Transcriptomic analysis using DESeq2 determined significance by using
860 Benjamini and Hochberg method-corrected Wald Test P values (Fig 2, Supplemental Data 1). P-
861 adj values of 0.1 or less were considered as hits for this analysis. The regression analysis to
862 compare known m⁶A modified sites (30) with DEG fold-change expression was done using

863 internal statistics tools in Graphpad Prism software to determine non-linear regression to a
864 second order polynomial (quadratic), to determine a best fit model to the data. A P-value of
865 <0.0001 and R-squared of 0.05239 was recorded for the alternative hypothesis (B0
866 unconstrained), and a R-squared value of -0.4864 was recorded for the null hypothesis (B0 = 0).
867 GSEA software was used for gene set enrichment analysis (70), and P-values are derived by
868 permutation using the standard 100 permutation default setting. We included data from gene-sets
869 reported with p-values over the significance cut off as well to give a more complete picture of
870 the pathways represented by significant DEGs, even when the number of related DEGs was
871 somewhat low for a pathway. P-values and number of DEGS found for each gene set listed are
872 shown in the figures (Fig. 2E,F). All graphs of plotted data were plotted in GraphPad Prism 10.

873 References

- 874 1. K. A. Berggren, R. E. Schwartz, R. E. Kleiner, A. Ploss, The impact of epitranscriptomic modifications on
875 liver disease. *Trends Endocrinol Metab* **35** (2024).
- 876 2. Y. Zou, G. Jiang, Y. Xie, H. Li, m6A-Related Genes Contribute to Poor Prognosis of Hepatocellular
877 Carcinoma. *Comput Math Methods Med* **2022** (2022).
- 878 3. X. Jiang, B. Liu, Z. Nie, L. Duan, Q. Xiong, Z. Jin, C. Yang, Y. Chen, The role of m6A modification in the
879 biological functions and diseases. *Signal Transduction and Targeted Therapy* **2021 6:1 6**, 1–16 (2021).
- 880 4. D. Yuan, S. Wang, S. Chen, S. People’s Hospital, J. Sun, P. Han, B. Xu, Y. Zhong, Z. Xu, P. Zhang, P. Mi,
881 C. Zhang, Y. Xia, S. Li, M. Heikenwalder, m6A modification-tuned sphingolipid metabolism regulates
882 postnatal liver development. doi: 10.21203/RS.3.RS-1372810/V1 (2022).
- 883 5. I. A. Roundtree, M. E. Evans, T. Pan, C. He, Dynamic RNA Modifications in Gene Expression Regulation.
884 *Cell* **169**, 1187–1200 (2017).
- 885 6. J. Huang, P. Yin, Structural Insights into N6-methyladenosine (m6A) Modification in the Transcriptome.
886 *Genomics Proteomics Bioinformatics* **16**, 85–98 (2018).
- 887 7. Z. Lv, R. Ran, Y. Yang, M. Xiang, H. Su, J. Huang, The interplay between N6-methyladenosine and
888 precancerous liver disease: molecular functions and mechanisms. *Discover. Oncology* **14** (2023).
- 889 8. J. Meng, Z. Zhao, Z. Xi, Q. Xia, Liver-specific Mettl3 ablation delays liver regeneration in mice. doi:
890 10.1016/j.gendis.2020.11.002 (2020).
- 891 9. J. M. Barajas, C. H. Lin, H. L. Sun, F. Alencastro, A. C. Zhu, M. Aljuhani, L. Navari, S. A. Yilmaz, L. Yu,
892 K. Corps, C. He, A. W. Duncan, K. Ghoshal, METTL3 Regulates Liver Homeostasis, Hepatocyte Ploidy,
893 and Circadian Rhythm-Controlled Gene Expression in Mice. *Am J Pathol* **192**, 56–71 (2022).
- 894 10. W. Xie, L. L. Ma, Y. Q. Xu, B. H. Wang, S. M. Li, METTL3 inhibits hepatic insulin sensitivity via N6-
895 methyladenosine modification of Fasn mRNA and promoting fatty acid metabolism. *Biochem Biophys Res*
896 *Commun* **518**, 120–126 (2019).
- 897 11. S. Wang, S. Chen, J. Sun, P. Han, B. Xu, X. Li, Y. Zhong, Z. Xu, P. Zhang, P. Mi, C. Zhang, L. Li, H.
898 Zhang, Y. Xia, S. Li, M. Heikenwalder, D. Yuan, m6A modification-tuned sphingolipid metabolism
899 regulates postnatal liver development in male mice. *Nature Metabolism* **2023 5:5 5**, 842–860 (2023).
- 900 12. B. J. Petri, M. C. Cave, C. M. Klinge, Changes in m6A in Steatotic Liver Disease. *Genes (Basel)* **14** (2023).
- 901 13. J. Luo, T. Xu, K. Sun, N6-Methyladenosine RNA Modification in Inflammation: Roles, Mechanisms, and
902 Applications. *Front Cell Dev Biol* **9** (2021).
- 903 14. X. Gan, Z. Dai, C. Ge, H. Yin, Y. Wang, J. Tan, S. Sun, W. Zhou, S. Yuan, F. Yang, FTO promotes liver
904 inflammation by suppressing m6A mRNA methylation of IL-17RA. *Front Oncol* **12**, 989353 (2022).
- 905 15. H. Imam, M. Khan, N. S. Gokhale, A. B. R. McIntyre, G. W. Kim, J. Y. Jang, S. J. Kim, C. E. Mason, S. M.
906 Horner, A. Siddiqui, N6-methyladenosine modification of hepatitis b virus RNA differentially regulates the
907 viral life cycle. *Proc Natl Acad Sci U S A* **115**, 8829–8834 (2018).
- 908 16. G.-W. Kim, J.-S. Moon, S. O. Gudima, A. Siddiqui, N 6 -Methyladenine Modification of Hepatitis Delta
909 Virus Regulates Its Virion Assembly by Recruiting YTHDF1 . *J Virol* **96** (2022).
- 910 17. G.-W. Kim, H. Imam, M. Khan, S. A. Mir, S.-J. Kim, S. K. Yoon, W. Hur, A. Siddiqui, HBV-Induced
911 Increased N6 Methyladenosine Modification of PTEN RNA Affects Innate Immunity and Contributes to
912 HCC. *Hepatology*, doi: 10.1002/hep.31313 (2020).

- 913 18. A. B. R. McIntyre, N. S. Gokhale, L. Cerchiatti, S. R. Jaffrey, S. M. Horner, C. E. Mason, Limits in the
914 detection of m6A changes using MeRIP/m6A-seq. *Scientific Reports* 2020 10:1 **10**, 1–15 (2020).
- 915 19. J. Liu, X. Dou, C. Chen, C. Chen, C. Liu, M. Michelle Xu, S. Zhao, B. Shen, Y. Gao, D. Han, C. He, N6-
916 methyladenosine of chromosome-associated regulatory RNA regulates chromatin state and transcription.
917 *Science* **367**, 580 (2020).
- 918 20. D. Yu, J. R. Horton, J. Yang, T. Hajian, M. Vedadi, C. A. Sagum, M. T. Bedford, R. M. Blumenthal, X.
919 Zhang, X. Cheng, Human MettL3-MettL14 RNA adenine methyltransferase complex is active on double-
920 stranded DNA containing lesions. *Nucleic Acids Res* **49**, 11629–11642 (2021).
- 921 21. S. Masuda, R. Das, H. Cheng, E. Hurt, N. Dorman, R. Reed, Recruitment of the human TREX complex to
922 mRNA during splicing. *Genes Dev* **19**, 1512 (2005).
- 923 22. D. Han, A. P. Longhini, X. Zhang, V. Hoang, M. Z. Wilson, K. S. Kosik, Dynamic assembly of the mRNA
924 m6A methyltransferase complex is regulated by METTL3 phase separation. *PLoS Biol* **20**, e3001535
925 (2022).
- 926 23. S. Lesbirel, N. Viphakone, M. Parker, J. Parker, C. Heath, I. Sudbery, S. A. Wilson, The m6A-methylase
927 complex recruits TREX and regulates mRNA export. *Scientific Reports* 2018 8:1 **8**, 1–12 (2018).
- 928 24. S. Lesbirel, S. A. Wilson, The m6A-methylase complex and mRNA export. *Biochimica et Biophysica Acta*
929 (*BBA*) - *Gene Regulatory Mechanisms* **1862**, 319–328 (2019).
- 930 25. A. M. Maldonado López, E. K. Ko, S. Huang, G. Pacella, N. Kuprasertkul, C. A. D'souza, R. A. Reyes
931 Hueros, H. Shen, J. Stoute, H. Elashal, M. Sinkfield, A. Anderson, S. Prouty, H. B. Li, J. T. Seykora, K. F.
932 Liu, B. C. Capell, Mettl3-catalyzed m6A regulates histone modifier and modification expression in self-
933 renewing somatic tissue. *Sci Adv* **9** (2023).
- 934 26. K. J. Yoon, F. R. Ringeling, C. Vissers, F. Jacob, M. Pokrass, D. Jimenez-Cyrus, Y. Su, N. S. Kim, Y. Zhu,
935 L. Zheng, S. Kim, X. Wang, L. C. Doré, P. Jin, S. Regot, X. Zhuang, S. Canzar, C. He, G. li Ming, H. Song,
936 Temporal Control of Mammalian Cortical Neurogenesis by m6A Methylation. *Cell* **171**, 877-889.e17
937 (2017).
- 938 27. C. Postic, M. Shiota, K. D. Niswender, T. L. Jetton, Y. Chen, J. M. Moates, K. D. Shelton, J. Lindner, A. D.
939 Cherrington, M. A. Magnuson, Dual roles for glucokinase in glucose homeostasis as determined by liver and
940 pancreatic beta cell-specific gene knock-outs using Cre recombinase. *J Biol Chem* **274**, 305–315 (1999).
- 941 28. T. G. Meng, X. Lu, L. Guo, G. M. Hou, X. S. Ma, Q. N. Li, L. Huang, L. H. Fan, Z. H. Zhao, X. H. Ou, Y.
942 C. OuYang, H. Schatten, L. Li, Z. B. Wang, Q. Y. Sun, Mettl14 is required for mouse postimplantation
943 development by facilitating epiblast maturation. *FASEB J* **33**, 1179–1187 (2019).
- 944 29. M. Li, X. Zhao, W. Wang, H. Shi, Q. Pan, Z. Lu, S. P. Perez, R. Suganthan, C. He, M. Bjørås, A.
945 Klungland, Ythdf2-mediated m6A mRNA clearance modulates neural development in mice. *Genome Biol*
946 **19** (2018).
- 947 30. Y. Tang, K. Chen, B. Song, J. Ma, X. Wu, Q. Xu, Z. Wei, J. Su, G. Liu, R. Rong, Z. Lu, J. P. de Magalhães,
948 D. J. Rigden, J. Meng, m6A-Atlas: a comprehensive knowledgebase for unraveling the N6-methyladenosine
949 (m6A) epitranscriptome. *Nucleic Acids Res* **49**, D134 (2021).
- 950 31. Y. Xu, Z. Zhou, X. Kang, L. Pan, C. Liu, X. Liang, J. Chu, S. Dong, Y. Li, Q. Liu, Y. Sun, S. Yu, Q. Zhang,
951 Mettl3-mediated mRNA m6A modification controls postnatal liver development by modulating the
952 transcription factor Hnf4a. *Nature Communications* 2022 13:1 **13**, 1–17 (2022).
- 953 32. N. Zhang, X. Tian, T. Yan, H. Wang, D. Zhang, C. Lin, Q. Liu, S. Jiang, Insights into the role of nucleotide
954 methylation in metabolic-associated fatty liver disease. *Front Immunol* **14** (2023).
- 955 33. Y. Luo, Z. Zhang, L. Xiang, B. Zhou, X. Wang, Y. Lin, X. Ding, F. Liu, Y. Lu, Y. Peng, Analysis of N6-
956 Methyladenosine Methylation Modification in Fructose-Induced Non-Alcoholic Fatty Liver Disease. doi:
957 10.3389/fendo.2021.780617.
- 958 34. G. Tong, X. Chen, J. Lee, J. Fan, S. Li, K. Zhu, Z. Hu, L. Mei, Y. Sui, Y. Dong, R. Chen, Z. Jin, B. Zhou, X.
959 Li, X. Wang, W. Cong, P. Huang, L. Jin, Fibroblast growth factor 18 attenuates liver fibrosis and HSCs
960 activation via the SMO-LATS1-YAP pathway. *Pharmacol Res* **178** (2022).
- 961 35. T. Chen, G. Dalton, S. H. Oh, R. Maeso-Diaz, K. Du, R. A. Meyers, C. Guy, M. F. Abdelmalek, R. Henao,
962 P. Guarnieri, S. S. Pullen, S. Gregory, J. Locker, J. M. Brown, A. M. Diehl, Hepatocyte Smoothed
963 Activity Controls Susceptibility to Insulin Resistance and Nonalcoholic Fatty Liver Disease. *Cell Mol*
964 *Gastroenterol Hepatol* **15**, 949–970 (2023).
- 965 36. M. Verdelho Machado, A. M. Diehl, The hedgehog pathway in nonalcoholic fatty liver disease. *Crit Rev*
966 *Biochem Mol Biol* **53**, 264 (2018).
- 967 37. M. Schuler, A. Dierich, P. Chambon, D. Metzger, Efficient temporally controlled targeted somatic
968 mutagenesis in hepatocytes of the mouse. *genesis* **39**, 167–172 (2004).

- 969 38. G. K. Michalopoulos, Liver regeneration. *J Cell Physiol* **213**, 286–300 (2007).
- 970 39. W. Pu, H. Zhu, M. Zhang, M. Pikiólek, C. Ercan, J. Li, X. Huang, X. Han, Z. Zhang, Z. Lv, Y. Li, K. Liu, L.
971 He, X. Liu, M. H. Heim, L. M. Terracciano, J. S. Tchorz, B. Zhou, Bipotent transitional liver progenitor
972 cells contribute to liver regeneration. *Nat Genet* **55**, 651–664 (2023).
- 973 40. Y. Nevzorova, R. Tolba, C. Trautwein, C. Liedtke, Partial hepatectomy in mice. *Lab Anim* **49**, 81–88
974 (2015).
- 975 41. K.-J. Yoon, F. R. Ringeling, C. Vissers, F. Jacob, M. Pokrass, D. Jimenez-Cyrus, Y. Su, N.-S. Kim, Y. Zhu,
976 L. Zheng, S. Kim, X. Wang, L. C. Doré, P. Jin, S. Regot, X. Zhuang, S. Canzar, C. He, G.-L. Ming, H.
977 Song, Temporal Control of Mammalian Cortical Neurogenesis by m6A Methylation. *Cell* **171**, 877–889.e17
978 (2017).
- 979 42. S. Geula, S. Moshitch-Moshkovitz, D. Dominissini, A. A. F. Mansour, N. Kol, M. Salmon-Divon, V.
980 Hershkovitz, E. Peer, N. Mor, Y. S. Manor, M. S. Ben-Haim, E. Eyal, S. Yunger, Y. Pinto, D. A. Jaitin, S.
981 Viukov, Y. Rais, V. Krupalnik, E. Chomsky, M. Zerbib, I. Maza, Y. Rechavi, R. Massarwa, S. Hanna, I.
982 Amit, E. Y. Levanon, N. Amariglio, N. Stern-Ginossar, N. Novershtern, G. Rechavi, J. H. Hanna, m6A
983 mRNA methylation facilitates resolution of naïve pluripotency toward differentiation. *Science (1979)* **347**,
984 1002–1006 (2015).
- 985 43. P. Tabnak, Y. Ghasemi, M. Natami, R. Khorram, M. Ebrahimnezhad, Role of m6A modification in
986 dysregulation of Wnt/ β -catenin pathway in cancer. *Biomedicine & Pharmacotherapy* **157**, 114023 (2023).
- 987 44. X. Cao, Y. Shu, Y. Chen, Q. Xu, G. Guo, Z. Wu, M. Shao, Y. Zhou, M. Chen, Y. Gong, C. Li, Y. Shi, H.
988 Bu, Mettl14-Mediated m6A Modification Facilitates Liver Regeneration by Maintaining Endoplasmic
989 Reticulum Homeostasis. *Cell Mol Gastroenterol Hepatol* **12**, 633 (2021).
- 990 45. I. Yang, S. Yeon Oh, S. Jang, I. Yong Kim, Y. Me Sung, J. Kyung Seong, Mettl14 mutation restrains liver
991 regeneration by attenuating mitogens derived from non-parenchymal liver cells. doi:
992 10.5483/BMBRep.2022.55.12.140.
- 993 46. A. Kasarinaite, M. Sinton, P. T. K. Saunders, D. C. Hay, The Influence of Sex Hormones in Liver Function
994 and Disease. *Cells* **12** (2023).
- 995 47. P. Fickert, U. Stöger, A. Fuchsbichler, T. Moustafa, H. U. Marschall, A. H. Weiglein, O. Tsybrovskyy, H.
996 Jaeschke, K. Zatloukal, H. Denk, M. Trauner, A New Xenobiotic-Induced Mouse Model of Sclerosing
997 Cholangitis and Biliary Fibrosis. *Am J Pathol* **171**, 525 (2007).
- 998 48. S. Dong, Q. L. Chen, Y. N. Song, Y. Sun, B. Wei, X. Y. Li, Y. Y. Hu, P. Liu, S. B. Su, Mechanisms of
999 CCl4-induced liver fibrosis with combined transcriptomic and proteomic analysis. *J Toxicol Sci* **41**, 561–572
1000 (2016).
- 1001 49. Y. Jiang, Q. Han, H. Zhao, J. Zhang, The Mechanisms of HBV-Induced Hepatocellular Carcinoma. *J*
1002 *Hepatocell Carcinoma* **8**, 435–450 (2021).
- 1003 50. C. Zhang, D. Dai, W. Zhang, W. Yang, Y. Guo, Q. Wei, Role of m6A RNA methylation in the development
1004 of hepatitis B virus-associated hepatocellular carcinoma. *J Gastroenterol Hepatol* **37**, 2039–2050 (2022).
- 1005 51. G.-W. Kim, A. Siddiqui, Hepatitis B virus X protein recruits methyltransferases to affect cotranscriptional
1006 N6-methyladenosine modification of viral/host RNAs. *Proceedings of the National Academy of Sciences*
1007 **118**, e2019455118 (2021).
- 1008 52. G. W. Kim, J. S. Moon, A. Siddiqui, N6-methyladenosine modification of the 5' epsilon structure of the
1009 HBV pregenome RNA regulates its encapsidation by the viral core protein. *Proc Natl Acad Sci U S A* **119**
1010 (2022).
- 1011 53. A. Ploss, H. Strick-Marchand, W. Li, Animal Models for Hepatitis B: Does the Supply Meet the Demand?
1012 *Gastroenterology* **160**, 1437–1442 (2021).
- 1013 54. J. M. Fustin, M. Doi, Y. Yamaguchi, H. Hida, S. Nishimura, M. Yoshida, T. Isagawa, M. S. Morioka, H.
1014 Kakeya, I. Manabe, H. Okamura, RNA-Methylation-Dependent RNA Processing Controls the Speed of the
1015 Circadian Clock. *Cell* **155**, 793–806 (2013).
- 1016 55. I. A. Roundtree, G. Z. Luo, Z. Zhang, X. Wang, T. Zhou, Y. Cui, J. Sha, X. Huang, L. Guerrero, P. Xie, E.
1017 He, B. Shen, C. He, YTHDC1 mediates nuclear export of N6-methyladenosine methylated mRNAs. *Elife* **6**
1018 (2017).
- 1019 56. X. Dou, L. Huang, Y. Xiao, C. Liu, Y. Li, X. Zhang, L. Yu, R. Zhao, L. Yang, C. Chen, X. Yu, B. Gao, M.
1020 Qi, Y. Gao, B. Shen, S. Sun, C. He, J. Liu, METTL14 is a chromatin regulator independent of its RNA N6-
1021 methyladenosine methyltransferase activity. *Protein Cell* **14**, 683–697 (2023).
- 1022 57. N. A. Zhigalova, K. Y. Oleynikova, A. S. Ruzov, A. S. Ermakov, The Functions of N6-Methyladenosine in
1023 Nuclear RNAs. *Biochemistry (Moscow) 2024 89:1* **89**, 159–172 (2024).

- 1024 58. V. Gupta, I. Gupta, J. Park, Y. Bram, R. E. Schwartz, Hedgehog Signaling Demarcates a Niche of
1025 Fibrogenic Peribiliary Mesenchymal Cells. *Gastroenterology* **159**, 624-638.e9 (2020).
- 1026 59. Q. Feng, D. Wang, T. Xue, C. Lin, Y. Gao, L. Sun, Y. Jin, D. Liu, The role of RNA modification in
1027 hepatocellular carcinoma. *Front Pharmacol* **13** (2022).
- 1028 60. Y. Du, Y. Ma, Q. Zhu, T. Liu, Y. Jiao, P. Yuan, X. Wang, An m6A-Related Prognostic Biomarker
1029 Associated With the Hepatocellular Carcinoma Immune Microenvironment. *Front Pharmacol* **12**, 1–16
1030 (2021).
- 1031 61. L. G. Guidotti, B. Matzke, H. Schaller, F. V Chisari, High-level hepatitis B virus replication in transgenic
1032 mice. *J Virol* **69**, 6158–6169 (1995).
- 1033 62. J. Schindelin, I. Arganda-Carreras, E. Frise, V. Kaynig, M. Longair, T. Pietzsch, S. Preibisch, C. Rueden, S.
1034 Saalfeld, B. Schmid, J. Y. Tinevez, D. J. White, V. Hartenstein, K. Eliceiri, P. Tomancak, A. Cardona, Fiji:
1035 an open-source platform for biological-image analysis. *Nature Methods* **2012 9:7 9**, 676–682 (2012).
- 1036 63. Y. Liu, H. Liu, Z. Hu, Y. Ding, X. Ben Pan, J. Zou, J. Xi, G. Yu, H. Huang, M. T. Luo, F. Guo, S. Liu, Q.
1037 Sheng, J. Jia, Y. T. Zheng, J. Wang, X. Chen, J. T. Guo, L. Wei, F. Lu, Hepatitis B Virus Virions Produced
1038 Under Nucleos(t)ide Analogue Treatment Are Mainly Not Infectious Because of Irreversible DNA Chain
1039 Termination. *Hepatology* **71**, 463–476 (2020).
- 1040 64. J. Wang, T. Shen, X. Huang, G. R. Kumar, X. Chen, Z. Zeng, R. Zhang, R. Chen, T. Li, T. Zhang, Q. Yuan,
1041 P. C. Li, Q. Huang, R. Colonno, J. Jia, J. Hou, M. A. McCrae, Z. Gao, H. Ren, N. Xia, H. Zhuang, F. Lu,
1042 Serum hepatitis B virus RNA is encapsidated pregenome RNA that may be associated with persistence of
1043 viral infection and rebound. *J Hepatol* **65**, 700–710 (2016).
- 1044 65. D. Alpern, V. Gardeux, J. Russeil, B. Mangeat, A. C. A. Meireles-Filho, R. Breysse, D. Hacker, B.
1045 Deplancke, BRB-seq: ultra-affordable high-throughput transcriptomics enabled by bulk RNA barcoding and
1046 sequencing. *Genome Biol* **20** (2019).
- 1047 66. E. V. Mesev, A. E. Lin, E. G. Guare, B. L. Heller, F. Douam, B. Adamson, J. E. Toettcher, A. Ploss,
1048 Membrane-proximal motifs encode differences in signaling strength between type I and III interferon
1049 receptors. *Sci Signal* **16** (2023).
- 1050 67. S. Picelli, Å. K. Björklund, B. Reinius, S. Sagasser, G. Winberg, R. Sandberg, Tn5 transposase and
1051 tagmentation procedures for massively scaled sequencing projects. *Genome Res* **24**, 2033–2040 (2014).
- 1052 68. Nuclei Isolation from Human Frozen Liver. <https://www.protocols.io/view/nuclei-isolation-from-human-frozen-liver-36wgq5keygk5/v1>.
- 1053 69. V. K. Mootha, C. M. Lindgren, K. F. Eriksson, A. Subramanian, S. Sihag, J. Lehar, P. Puigserver, E.
1054 Carlsson, M. Ridderstråle, E. Laurila, N. Houstis, M. J. Daly, N. Patterson, J. P. Mesirov, T. R. Golub, P.
1055 Tamayo, B. Spiegelman, E. S. Lander, J. N. Hirschhorn, D. Altshuler, L. C. Groop, PGC-1 α -responsive
1056 genes involved in oxidative phosphorylation are coordinately downregulated in human diabetes. *Nature*
1057 *Genetics* **2003 34:3 34**, 267–273 (2003).
- 1058 70. A. Subramanian, P. Tamayo, V. K. Mootha, S. Mukherjee, B. L. Ebert, M. A. Gillette, A. Paulovich, S. L.
1059 Pomeroy, T. R. Golub, E. S. Lander, J. P. Mesirov, Gene set enrichment analysis: A knowledge-based
1060 approach for interpreting genome-wide expression profiles. *Proc Natl Acad Sci U S A* **102**, 15545–15550
1061 (2005).
- 1062 71. J. M. Gaska, L. Parsons, M. Balev, A. Cirincione, W. Wang, R. E. Schwartz, A. Ploss, Conservation of cell-
1063 intrinsic immune responses in diverse nonhuman primate species. *Life Sci Alliance* **2** (2019).
- 1064 72. C. Stringer, T. Wang, M. Michaelos, M. Pachitariu, Cellpose: a generalist algorithm for cellular
1065 segmentation. *Nature Methods* **2020 18:1 18**, 100–106 (2020).
- 1066 73. B. Aigouy, D. Umetsu, S. Eaton, Segmentation and Quantitative Analysis of Epithelial Tissues. *Methods*
1067 *Mol Biol* **1478**, 227–239 (2016).
- 1068
- 1069

1070 Acknowledgments

1071 We thank Dr. Gary Laevsky and Sha Wang of the Princeton Imaging Core which is a Nikon
1072 Center of Excellence, Christina de Coste of the Flow cytometry Core and Dr. Wei Wang of the
1073 Genomics core for outstanding technical support. We are grateful to Dr. Frank Chisari (Scripps
1074 Research) for generously sharing the 1.3x HBV tg mice, Dr. Chuan He (University of
1075 Chicago/HHMI) for kindly providing the Ythdf1^{-/-}, Ythdf2^[fl/fl], and Mettl14^[fl/fl] and Dr. Pierre
1076 Chambon (INSERM) for the Alb-ERT2-Cre mouse lines. We further thank Dr. Yuri Pritykin for

1077 useful discussion of the RNAseq data analysis and all members of the Ploss lab for critical
1078 discussion of the study and manuscript.

1079

1080 **Funding:**

- 1081 • National Institute of Allergy and Infectious Diseases (NIAID)
- 1082 ○ R01 AI138797 (to A.P.)
- 1083 ○ R01 AI153236 (to A.P.)
- 1084 ○ R01 AI146917 (to A.P.)
- 1085 ○ R01 AI168048 (to A.P.)
- 1086 ○ R01 AI107301(to A.P.)
- 1087 • National Institute of Digestive Diseases and Kidney (NIDDK)
- 1088 ○ R01DK121072 (to R.E.S.)
- 1089 • National Institutes of Health Office of the Director
- 1090 ○ S10-OD026983 (to N.A.C.)
- 1091 ○ SS10-OD030269 (to N.A.C.)
- 1092 • National Institute of General Medical Sciences (NIGMS)
- 1093 ○ Predoctoral training grant T32GM007388 (to K.A.B., M.P.S., S.M.)
- 1094 • National Cancer Institute
- 1095 ○ P30CA072720
- 1096 • Burroughs Welcome Fund
- 1097 ○ Investigators in Pathogenesis award 101539 (to A.P.)
- 1098 • Damon Runyon Cancer Research Foundation
- 1099 ○ Postdoctoral fellowship DRG-2432-21 (to A.E.L.)
- 1100 • New Jersey Commission on Cancer Research (NJCCR)
- 1101 ○ Postdoctoral fellowship COCR24PDF002 (to Y.L.)
- 1102 ○ Predoctoral fellowship COCR23PRF008 (to S.M.)
- 1103 • Princeton University Catalysis Initiative (to A.P. and R.K.)

1104

1105 **Author contributions:**

1106 Conceptualization: KAB, AP

1107 Methodology: KAB, AP

1108 Investigation: KAB, SS, AEL, MPS, SM, TRC, YL, HPG, SS, ARB, SC, BH, NH, QA

1109 DB, DW, JMC, AP

1110 Visualization: KAB, SS, AEL

1111 Supervision: AP, RES, NAC, REK, JMC

1112 Writing—original draft: KAB, AP

1113 Writing—review & editing: All authors

1114

1115 **Competing interests**

1116 All authors declare they have no competing interests.

1117

1118 **Data and materials availability:** 1.3x HBV tg mice are available under MTA from Dr.
1119 Frank Chisari (Scripps Research), the *Ythdf1*^{-/-}, *Ythdf2*^[fl/fl], and *Mettl14*^[fl/fl] under MTA
1120 from Dr. Chuan He (University of Chicago/HHMI) and the Alb-ERT2-Cre mouse lines
1121 under MTA from Dr. Pierre Chambon.

1122

1123 All data are available in the main text or the supplementary materials. Raw RNA-Seq
1124 reads and the processed counts matrix can be accessed at NCBI GEO accession:
1125 GSE265879.